

UPPSALA UNIVERSITY

ERASMUS+ SEMESTER 08/2020 – 01/2021

MASTER PROJECT IN PHYSICS AND MATERIALS SCIENCE (30 CP)

Project report

Phonon-modulated x-ray absorption in SrTiO_3

Jonas Hoecht

Supervisors: Dr. Oscar Grånäs & Dr. Patrik Thunström & Prof. Dr.
Olle Eriksson, Div. of Materials theory, Uppsala University,
and

Prof. Dr. Maurits Haverkort, Institute for Theoretical Physics,
Heidelberg University.

Subject reader: Dr. Sergei Butorin, Div. of Molecular and Condensed
Matter Physics, Uppsala University.

Examiner: Prof. Dr. Susanne Mirbt, Div. of Materials theory,
Uppsala University.



Phonon-modulated x-ray absorption in SrTiO_3

Jonas Hoecht

08/2020 – 01/2021

Abstract:

The aim of this work is to predict the influence of phonon modulations (Kozina *et al.* 2019 [1]) on the x-ray absorption near-edge fine structure of the Ti-L_{2,3}-edge (Yamaguchi *et al.* 1982 [2], Thole *et al.* 1985 [3], De Groot 1990 [4]) in cubic SrTiO₃. Employing Density Functional Theory in combination with Multiplet Ligand Field Theory (Haverkort *et al.* 2012 [5], Luder *et al.* 2017 [6]), previous experimental and theoretical data on the octahedrally symmetric structure are reproduced with good agreement. Phonon modulations with a maximum atomic displacement of 5% of the lattice parameter are shown to cause polarization-dependent changes in the x-ray absorption spectra just within reach of experimental resolution. This is suggested to reflect the strong susceptibility of the electronic structure to collective lattice excitations in SrTiO₃.

Contents

1	Introduction	4
1.1	Predicting properties of real materials	4
1.2	Phonon modulations in SrTiO_3	5
1.3	X-ray absorption spectroscopy	6
1.4	Outline of this work	7
2	Theoretical background	8
2.1	<i>Ab initio</i> -foundation: Density Functional Theory	10
2.2	Beyond the mean-field approximation: Many-body theory for correlated materials	12
2.2.1	Second Quantization	12
2.2.2	Green's functions in operator theory	14
2.2.3	Single Impurity Anderson Model	16
2.3	Calculation of observables: Linear Response Theory	18
2.3.1	Green's functions as correlation functions	18
2.3.2	Transition rate in an external field	21
2.4	Phonons and electron-phonon coupling	23
3	Computational Methods	24
3.1	RSPt	24
3.2	rspt2spectra	24
3.3	impurityModel	24
4	Results and Discussion	25
4.1	Density of states	26
4.2	Phonon spectrum and lattice modulation	27
4.3	Discretization of the hybridization function	29
4.4	X-ray absorption spectra	31
4.5	Experimental applications	34
5	Conclusion	34

1 Introduction

1.1 Predicting properties of real materials

It seems to be a deep-rooted instinct of mankind to try and understand the matter which surrounds us, in order to eventually use this knowledge as a source of technological progress. The materials we use dominantly shape the world around us to the extent that we even use their names (stone, bronze, iron, glass, steel, maybe even plastic and carbon) to define historical ages [7].

Now that the experimental and theoretical tools for investigation of condensed matter on the microscopic level have been available for a century, the prediction of arbitrary macroscopic observables from first microscopic principles (*ab initio*) has become one of the central goals in materials theory. As a by-product of the intrinsic motivation to discover the fundamental reasons for our perception of the material world, *ab initio* predictions have yielded direct applications, such as Tunnel Magneto-Resistance (TMR) [8] with tremendous technological relevance for read-heads in hard disk drives [9]. Numerical simulations of condensed matter with increasing complexity are an important contribution to the development of novel materials, e.g. for sustainable energy solutions [10].

Even though the microscopic principles in materials theory are very well known in form of a Hamiltonian, and successful mean-field approximations exist, the treatment of strong Coulomb interaction in many-body systems still remains an only partially resolved challenge [11, Preface].

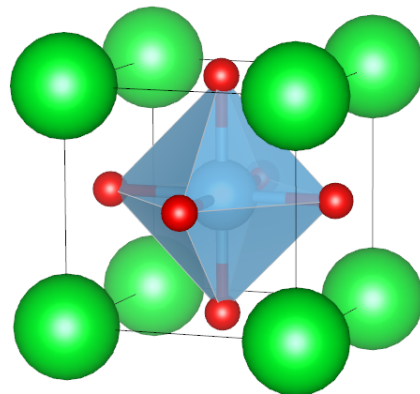


Figure 1.1: Crystal structure of STO. Left: Sample of natural STO in form of the mineral Tausonite [12]. Pure synthetics are usually transparent. Right: Unit cell of cubic STO [13] drawn with VESTA [14]. Sr: green, Ti: blue, O: red, cubic lattice constant: 3.9 Å.

1.2 Phonon modulations in SrTiO₃

SrTiO₃ (STO, Figure 1.1) has recently gained increasing attention in the materials theory community due to its interesting properties arising from the interplay of strongly correlated electrons and phonons. For instance, there is evidence of a cooperative effect at the FeSe/STO-interface, suggesting that the coupling of STO phonons to electrons in FeSe leads to an increase in the FeSe superconducting transition temperature to as high as 75 K [15].

STO occurs naturally in form of the mineral Tausonite. At room temperature, it has a cubic perovskite structure with a structural phase transition to a tetragonal structure below 105K [13]. Experimentally, it is now possible to drive phonon modes in STO by using electric fields in the THz regime as pump pulses [1]. The modulation of the electronic structure in reaction to the coherent distortions in the lattice can then be probed with a separate pulse as illustrated in Figure 1.2. This setup can be used to investigate the coupling of electronic properties of STO to the lattice in order to gain a better understanding of the microscopic reasons for the remarkable properties of this material.

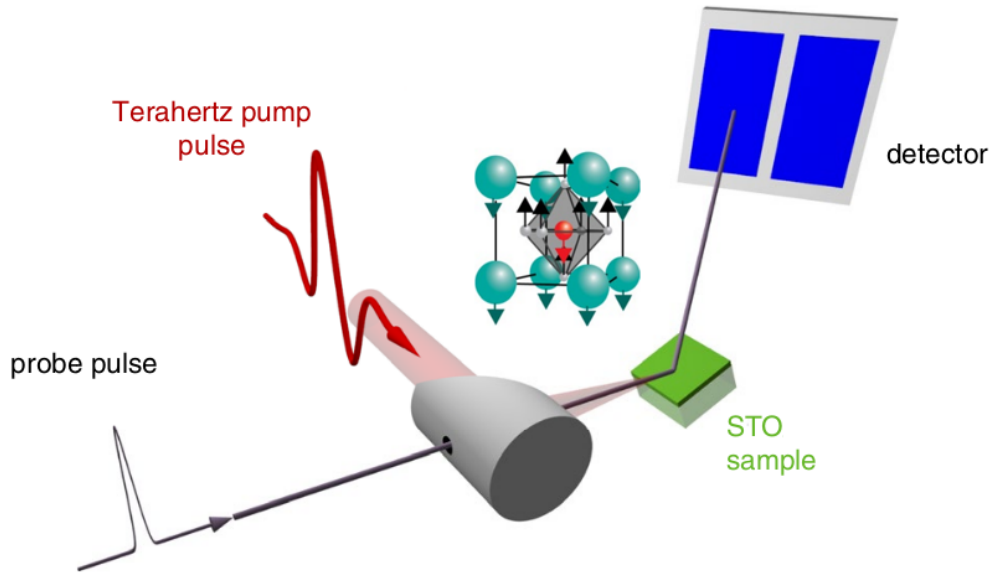


Figure 1.2: Schematic illustration of an experimental pump-probe setup (adapted from [1, Figure 1]). Phonons in a sample of STO are excited with a THz pump pulse with the effect of distorting the lattice coherently. Electronic degrees of freedom are then addressed with a separate probe pulse and the response of the material is observed.

It will be argued in Section 2.3.1 about Linear Response Theory that even though the electronic structure is driven out of equilibrium by the probe pulse, the response of the system can be approximated in terms of equilibrium expectation values for small enough field intensities.

The experimental *pump*-probe setup, however, introduces an additional temporal aspect to the problem, as the sample is driven out of equilibrium also by the previous pump pulse. As a first (adiabatic) approximation, one can argue that the time-scales of lattice and electronic excitations are separated by the large mass of the nuclei in comparison to electrons, $\frac{M}{m} \sim 10^3$. For the purpose of this study, it will hence be assumed that despite the presence of the pump, the electronic structure is always in equilibrium. The response of the sample to the electronic probe should in consequence reflect the equilibrium electronic structure for a coherently distorted lattice geometry.

1.3 X-ray absorption spectroscopy

One experimentally relevant and theoretically interesting way to probe the electronic structure of transition metal compounds such as STO is x-ray absorption spectroscopy (XAS), as reviewed e.g. in [16]. The XA process for the 2p→3d (L-edge) transition investigated here is sketched in Figure 1.3.

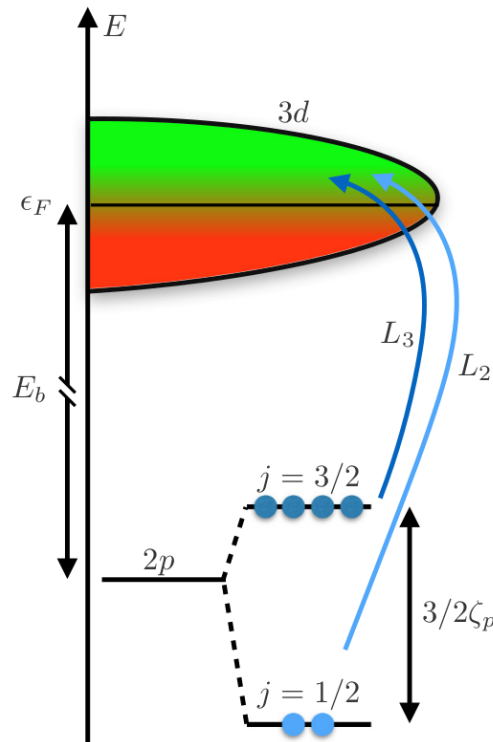


Figure 1.3: XA process 2p→3d (L-edge). In a simplified one-electron picture, an electron from the well-localized 2p core states is excited to the unoccupied part of the 3d band of the material by absorption of an x-ray photon. Through relativistic spin-orbit-coupling of strength ζ_p , the 2p initial states are split into $j = 1/2$ and $j = 3/2$ levels [6, Figure 1].

Experimentally, XA spectra can be measured indirectly by recording energy-resolved beam intensities before and after the sample (transmission mode) or by detecting decay products of the core-hole created in the absorption process (e.g. Auger electron yield, fluorescence yield). Due to the strong dependence of the absorption energy E_b on atomic number, XAS is an element-selective technique. In addition, the shape of the spectrum probes local symmetry and nominal oxidation state of the selected site [4].

In a one-electron picture, XAS should measure the unoccupied density of states (green area in Figure 1.3) of a material for photon energies exceeding E_b . However, electronic correlations become particularly important for transition metal compounds such as STO in presence of a core-hole: Because of the available phase-space for electron-electron scattering, the central argument of Fermi-liquid theory [17, Section 1.1] is not applicable, mean-field approaches fail, and a true many-body description is needed to predict the spectra of these so called *strongly correlated* materials.

1.4 Outline of this work

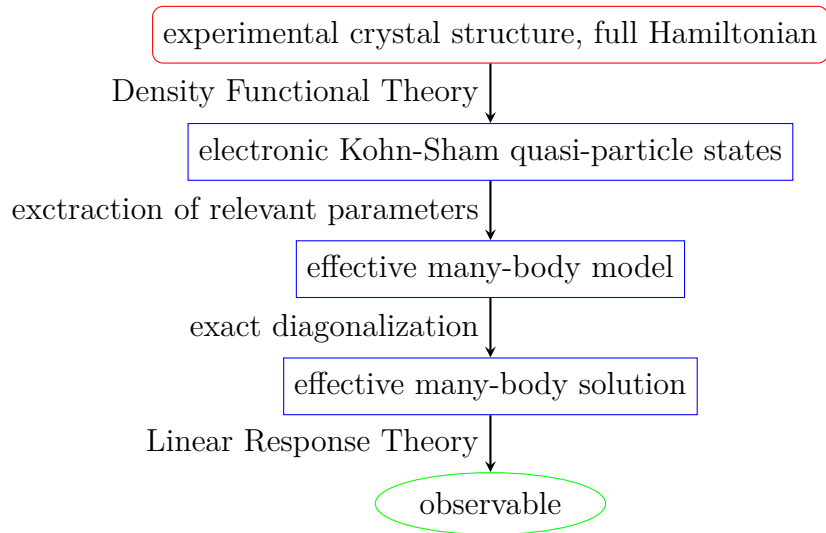


Figure 1.4: Workflow-diagram illustrating the research strategy [5, 6] applied in this work.

The aim of this work is the prediction (Section 1.1) of a direct experimental observable (the x-ray absorption spectrum, Section 1.3) for a real material (STO, Section 1.2) from microscopic principles. In particular, the influence of phonons on the $L_{2,3}$ -edge of Ti in STO (nominally d^0 -configuration) will be investigated. Central research questions are: Are the approximations made in this theoretical work adequate to reproduce previously established knowledge about STO and its spectrum? Can the electronic effect of the atomic displacement caused by driving a phonon mode in STO [1] be probed with XAS?, Is the adiabatic approximation (frozen phonons)

sufficient to predict XAS or other probes of the modified electronic structure?

In order to address these questions, this report aims to guide through the work-flow diagram sketched in Figure 1.4. The research strategy is adapted from [6], which is based on the Multiplet Ligand Field Theory (MLFT) [5] approach to predict XAS of transition metal compounds.

Starting from the experimental crystal structure and the full electronic Hamiltonian, Density Functional Theory (DFT, Section 2.1) will be used to obtain a mean-field description of the electronic structure in terms of Kohn-Sham quasi-particle states. This level of approximation will be further used to obtain parameters (Section 2.2.1) for an effective many-body model (Section 2.2.3). For the concrete application in this work, the fact that the hole in XAS is created in a state localized around a specific site is of great importance: The dimensionality of the many-body-problem can thus be reduced to a level that is tractable by exact diagonalization. All remaining sites, for which the influence of interaction on the final results is only marginal, will be treated within the mean-field approach. Having the effective many-body solution available, the observable of interest (here XAS), can be calculated using Linear Response Theory (Section 2.3.2).

All these aspects will be addressed from a theoretical perspective in Section 2, and the underlying theory of statistical quantum mechanics, Green’s functions, linear response, phonons and electron-phonon coupling will be summarized on the way.

Section 3 describes the computational implementation and lists the parameters used to obtain the results presented and discussed in Section 4.

2 Theoretical background

The general Hamiltonian in a condensed matter system in non-relativistic, adiabatic (Born-Oppenheimer) approximation is given by [18, Section 2.1]

$$\tilde{H} = -\frac{\hbar^2}{2m_e} \sum_i \nabla_{\tilde{r}_i}^2 + \frac{e^2}{4\pi\epsilon_0} \left[\frac{1}{2} \sum_{i \neq j} \frac{1}{|\tilde{r}_i - \tilde{r}_j|} - \sum_{i,I} \frac{Z_I}{|\tilde{r}_i - \tilde{R}_I|} + \frac{1}{2} \sum_{I \neq J} \frac{Z_I Z_J}{|\tilde{R}_I - \tilde{R}_J|} \right], \quad (2.1)$$

with a sum over all electrons i , and nuclei I in the system. This operator generates the electronic dynamics of the system prepared in the many-body-state $|\tilde{\psi}(T)\rangle$ through the Schrödinger equation (e.g. [19, §15])

$$i\hbar \frac{d}{dT} |\tilde{\psi}(T)\rangle = \tilde{H} |\tilde{\psi}(T)\rangle. \quad (2.2)$$

To choose convenient units, measure positions in units of a , *i.e.* $r = \frac{\tilde{r}}{a}$, and divide (2.2) by the suggested energy scale $\rho = \frac{\hbar^2}{2m_e a^2}$ to obtain

$$i \frac{d}{dt} |\psi(t)\rangle = H |\psi(t)\rangle, \quad (2.3)$$

with the dimensionless Hamiltonian $H = \frac{1}{\rho} \tilde{H}$, time variable $t = \frac{\hbar}{\rho} T$, and $\psi(t) = \tilde{\psi}(T)$. With the convenient choice $a = 4\pi\epsilon_0 \frac{\hbar^2}{e^2 m_e}$ (Bohr radius), the Hamiltonian thus reduces to

$$\begin{aligned} H &= -\frac{1}{2} \sum_i \nabla_{r_i}^2 + \frac{1}{2} \sum_{i \neq j} \underbrace{\frac{1}{|r_i - r_j|}}_{=w(i,j)} - \underbrace{\sum_{i,I} \frac{Z_I}{|r_i - R_I|}}_{=\sum_i v_{ext}(r_i)} + \frac{1}{2} \sum_{I \neq J} \underbrace{\frac{Z_I Z_J}{|R_I - R_J|}}_{\text{irrelev. constant}} \\ &\equiv T + W + V_{\text{ext}}, \end{aligned} \quad (2.4)$$

measuring energy¹ in units of $\rho = 2\text{Ry} = 2 \times 13.6\text{eV}$ (Hartree atomic units [20, Section 3.1]).

This system of natural units also ensures that limits can be taken in a well-defined way. The notation $t \rightarrow \infty$ (or in words ‘large t ’) for a dimensionless external time variable t , for instance, means in physical language $T \gg \tau$, *i.e.* the external time is large compared to the natural time-scale of the system.

Relativistic corrections to the Hamiltonian (2.4), most importantly relativistic kinetic energy, Darwin-term, and spin-orbit coupling, can be derived from the fully relativistic Dirac-equation in the non-relativistic limit (e.g. [21, Section 2.2]). To keep the notation compact here, only the spin-orbit coupling ξls will be explicitly added later. This correction becomes especially important for core orbitals of heavy elements, for which the radial change in the potential is large.

In the framework of quantum statistical mechanics, outcomes of measurements in equilibrium can be calculated as thermal expectation values of observables A : $\langle A \rangle = \text{Tr}\{\rho A\}$ with $\rho = Z^{-1} e^{-\beta H}$, $Z = \text{Tr}\{e^{-\beta H}\}$ [22, Chapter 8]. The trace is most easily evaluated in the many-body eigenbasis of H , which means that once the spectral problem $H |\psi\rangle = E |\psi\rangle$ is solved, all measurement outcomes in equilibrium can be predicted in principle. Due to the high dimensionality of the problem (even in discretized, periodic space), diagonalizing the full many-body Hamiltonian is however intractable and one has to rely on approximations in practice [20, Section 1].

¹The inter-ion potential has been discarded here as an irrelevant constant contribution to the total energy, but will be addressed again in Section 2.4 on phonons.

2.1 *Ab initio*-foundation: Density Functional Theory

Density Functional Theory (DFT) in the formulation by Kohn and Sham is a successful method to approach the complicated quantum-many-body problem on the mean-field level [20, Section 6]. DFT is based on the discovery by Hohenberg and Kohn [23] that the ground state electron-density $n_0(r) = |\psi_0(r)|^2$ uniquely determines V_{ext} , hence the full Hamiltonian (2.4), and in extension all properties of the specific condensed matter system. In addition, the ground state electron-density can be determined from minimization of a nonlocal and nonlinear energy functional $E[n]$ of the electron density. The energy functional $E[n]$ is independent of V_{ext} and in this sense universal.

The proofs of the Hohenberg-Kohn theorems (e.g. [20, Section 6.2]) are not constructive in a mathematical sense, *i.e.* only existence of a universal functional is proven, but an explicit expression is not derived. In general, the energy functional can be written as

$$E[n] = \underbrace{T[n] + W[n]}_{=F[n]} + \underbrace{\int_r dr V_{\text{ext}}(r)n(r)}_{=V_{\text{ext}}[n]}, \quad (2.5)$$

$$F[n] = T_S[n] + \frac{1}{2} \int_{r,r'} dr dr' \frac{n(r)n(r')}{|r - r'|} + E_{\text{xc}}[n], \quad (2.6)$$

where T_S is the kinetic energy of a hypothetical non-interacting electron gas, and the classical Coulomb interaction has been written explicitly to isolate any remaining exchange-correlation contributions.

For instance, one can use the local density approximation (LDA) [18, Section 2.3.3],

$$E_{\text{xc}}[n] = \int_r dr n(r)e_{\text{xc}}(n), \quad (2.7)$$

where e_{xc} is the exchange and correlation energy per particle of a homogeneous electron gas with density n , for which explicit expressions exist.

The density-functional for the single-particle kinetic energy $T_S[n]$, however, is not known explicitly [18, Section 2.3.1]. If one tries to map the problem onto an auxiliary system of non-interacting quasi-particles following the idea of Kohn and Sham ([24], reviewed e.g. in [20, Section 7]) the variational procedure can be executed nevertheless. In the auxiliary system, the energy functional is given by [18, Section 2.3.2]

$$E[n] = T_S[n] + \int_r dr V_{\text{eff}}(r)n(r), \quad (2.8)$$

$$V_{\text{eff}} = V_{\text{ext}} + \int_{r'} dr' \frac{n(r')}{|r - r'|} + \frac{\delta E_{\text{xc}}[n]}{\delta n(r)}. \quad (2.9)$$

This transforms the complicated many-body problem into an effective single-particle formulation in terms of non-interacting quasi-particles in an effective potential, which is also the reason why

DFT is called a mean field technique in this thesis. Upon variation of the energy functional [18, Section 2.3.2], one obtains the self-consistent² Schrödinger-like Kohn-Sham equation for the quasi-particle orbitals $|\psi_i\rangle$,

$$h^{MF} |\psi_i\rangle = \left[-\frac{1}{2} \nabla^2 + V_{\text{eff}} \right] |\psi_i\rangle = \epsilon_i |\psi_i\rangle. \quad (2.10)$$

In extended solids, one can exploit periodicity to further simplify these equations. Bloch's theorem, e.g. [25, Section 8], guarantees that solutions obey the property:

$$\psi(r + R) = e^{ikR} \psi(r) \quad (2.11)$$

for any lattice vector R . The quasi-momentum k can be taken as a label for the states, and all other degrees of freedom can be absorbed in the index n . One searches for a labelled eigenbasis $|\psi_{n,k}\rangle$.

In order to solve (2.10) with $i = (n, k)$ and $\langle \psi_{nk} | \psi_{n'k'} \rangle = \delta_{nk, n'k'}$ numerically for a given k -point, expand the quasiparticle states in a basis $|\chi_L\rangle$,

$$|\psi_{nk}\rangle = \sum_L c_{L,nk} |\chi_L\rangle, \quad (2.12)$$

thereby obtaining the standard homogeneous linear matrix equation

$$\sum_L \langle \chi_L | [h^{MF} - \epsilon_{nk}] | \chi_{L'} \rangle c_{L,nk} = 0. \quad (2.13)$$

One example of a possible basis are the linearized muffin-tin orbitals (LMTO) [20, Section 17.5]. The basic idea is to divide space in atomic-like regions of radius R_{MT} and interstitial regions, thereby reproducing the form of a muffin-tin in 2D. The basis is chosen to consist of states that are solutions to an atomic Schrödinger equation inside the tin (MT heads), and solutions to the free Helmholtz equation (tails) in the interstitial region. The two parts of the wave-function need to be matched at the sphere boundaries. The basis $|\chi_L\rangle$ can be labelled by $L = (R, \tau, \xi, \kappa)$, $\xi = (\nu, m, l, \sigma)$, where R is the lattice site, τ the basis vector within the unit cell, (ν, m, l) atomic quantum numbers for the head, σ the spin index, and κ defines the kinetic energy of the tail. Note that this basis is manifestly energy-dependent, but it can be linearized in energy to make the calculations computationally efficient. An advantage of this choice is that the basis functions are quite similar to the expected self-consistent solution, so that a small basis set is sufficient to make successful predictions [18, Section 5.1.6]. A detailed discussion of LMTO can be found in [20, Sections 16,17], and details on the implementation in RSPt are given in [18, Sections 5,6].

²Note that V_{eff} depends on the solutions $|\psi_i\rangle$ through the density $n_0(r) = \sum_i |\psi_i(r)|^2$.

After solution of (2.13) in a self-consistent cycle, a set of quasiparticle orbitals and corresponding energies, $(\epsilon_{nk}, \psi_{nk})$, is obtained, where the map $nk \mapsto \epsilon_{nk}$ is referred to as *band structure*. From this, several standard properties can be calculated [18, Section 4.4]:

The *density of states* (DOS) is a measure for the number of states at energy ω :

$$D(\omega) = \sum_{nk} \delta(\omega - \epsilon_{nk}). \quad (2.14)$$

To analyse the contribution of specific states $|\phi\rangle$ to the total DOS, one can define the projected density of states

$$pD_\phi(\omega) = \sum_{nk} |\langle \phi | \psi_{nk} \rangle|^2 \delta(\omega - \epsilon_{nk}), \quad (2.15)$$

where the choice $|\phi\rangle = |mk'\rangle$ and summation over mk' recovers the total DOS

$$\sum_{mk'} pD_{mk'}(\omega) = \sum_{mk'} \sum_{nk} \delta_{mk',nk} \delta(\omega - \epsilon_{nk}) = \sum_{nk} \delta(\omega - \epsilon_{nk}) = D(\omega). \quad (2.16)$$

In particular, partial summation over k for selected n is possible in order to isolate the contribution of a specific band.

Having a total of N electrons in the system, the *Fermi-energy* is determined as the largest energy with occupied states at zero temperature,

$$N = \int_{-\infty}^{E_F} D(\omega) d\omega. \quad (2.17)$$

2.2 Beyond the mean-field approximation: Many-body theory for correlated materials

Since the many-body problem has already been solved on a mean-field level by DFT, it can be hoped that the quasiparticle states found there are a good starting point for the construction of an effective many-body model. In order to keep this problem tractable, only a limited number of states can be taken into account in this model, selected depending on the question of interest.

2.2.1 Second Quantization

In order to benefit from the full beauty of the available mathematical formalism, it is convenient to work in a localized orthonormal basis $|i, \xi\rangle$. E.g., project onto the MT head [26, Section 3] of the LMTO basis $|R, \tau, \xi, \kappa\rangle$ introduced in Section 2.1. In real space coordinates \vec{r} , with spherical coordinates around the origin of the MTs, $\vec{r}_i = \vec{r} - \vec{R}_i = (r_i, \theta_i, \phi_i)$, and with $\xi = (\nu, l, m, \sigma)$,

$$\psi_{i,\xi}(\vec{r}) = \langle \vec{r} | i, \xi \rangle = \begin{cases} f_{\nu,l,\sigma}(r_i) Y_{l,m}(\theta_i, \phi_i), & r_i < R_{MT}, \\ 0, & \text{otherwise,} \end{cases} \quad (2.18)$$

where the solution has been decomposed in a radial part f and a spherical harmonic Y . To simplify the notation in what follows, a single multi-index i will be used for this new single-particle basis, $|i, \xi\rangle \rightarrow |i\rangle$.

In the notation of second quantization (e.g. [27, Section 6], [28, Section 1]), one can introduce fermionic creation and annihilation operators a_i^\dagger, a_i , with $[a_i, a_j^\dagger]_+ = \delta_{ij}$ and $[a_i, a_j]_+ = 0$, for correctly symmetrized many-mody states resulting from this single-particle basis.

On the constructed Fock space, any (correctly symmetrized) operator $H = \sum_i h_i^{(1)} + \frac{1}{2} \sum_{i \neq j} h_{ij}^{(2)}$ up to two-particle order can be expressed as

$$H = \sum_{ij} t_{ij} a_i^\dagger a_j + \frac{1}{2} \sum_{ijkl} U_{ijkl} a_i^\dagger a_j^\dagger a_l a_k, \quad (2.19)$$

$$t_{ij} = \langle i | H | j \rangle = \int_r dr \psi_i^*(r) h^{(1)}(r) \psi_j(r), \quad (2.20)$$

$$U_{ijkl} = \langle ij | H | kl \rangle = \int_{r, r'} dr dr' \psi_i^*(r) \psi_j^*(r') h^{(2)}(r, r') \psi_k(r) \psi_l(r'). \quad (2.21)$$

For the special case of Coulomb interaction with $h_{ij}^{(2)} = w(i, j) = \frac{1}{|r_i - r_j|}$, U_{abcd} can be expressed in terms of integrals over spherical harmonics, called *Gaunt coefficients* $c^k(l, m; l', m')$, and radial integrals $R^k(n_a l_a, n_b l_b, n_c l_c, n_d l_d)$ [29, Section 2.5.2]³:

$$U_{abcd} = \delta_{m_a+m_b, m_c+m_d} \sum_{k=0}^{k_{\max}} c^k(l_a, m_a; l_c, m_c) R^k(n_a l_a, n_b l_b, n_c l_c, n_d l_d) c^k(l_d, m_d; l_b, m_b), \quad (2.22)$$

$$c^k(l, m; l', m') = \sqrt{\frac{4\pi}{2k+1}} \int_0^{2\pi} d\phi \int_{-1}^1 d(\cos \theta) Y_{l,m}^*(\theta, \phi) Y_{k, m-m'} Y_{l', m'}(\theta, \phi), \quad (2.23)$$

$$R^k(n_a l_a, n_b l_b, n_c l_c, n_d l_d) = \int_0^\infty r^2 dr \int_0^\infty r'^2 dr' f_{n_a, l_a}(r) f_{n_b, l_b}(r') \frac{r^k}{r^{k+1}} f_{n_c, l_c}(r) f_{n_d, l_d}(r'), \quad (2.24)$$

with $k_{\max} = \min(|l_a + l_c|, |l_d + l_b|)$ and $r_{<(>)} = \min(r, r')$ ($\max(r, r')$).

After considering all constraints in the above equations, the interaction can be described by a finite number of Slater-Condon parameters of the form

$$\begin{aligned} F^k(nl, n'l') &= R^k(nl, n'l', nl, n'l'), \\ G^k(nl, n'l') &= R^k(nl, n'l', n'l', nl), \end{aligned} \quad (2.25)$$

for Coulomb and exchange integrals respectively. If the principal quantum number n is clear from the context, it will be left out of the notation, $F_{ll'}^k = F^k(nl, n'l')$.

If part of the interaction is already taken into account in $h^{(1)}$ on the mean-field level (DFT), it is necessary to subtract this part when correlations are added in order to avoid double-counting.

³Note that the convention for the interaction integral (2.21) is in agreement with RSPt conventions [18], but reversed w.r.t. [29], $U_{abcd} \leftrightarrow U_{abdc}$.

Since the energy functional in DFT is nonlinear, it is a nontrivial and basis-dependent task to decide which part of the interaction has effectively been taken into account. In this thesis, the multiplet ligand field theory formula [6, Appendix B]

$$\Sigma_{DC} = n_d U_{dd} + n_p U_{pd} - \delta_{CT} \quad (2.26)$$

is used, where n_d is the occupation of the d-orbitals, $n_p = 6$ is the occupation of the p orbitals, U_{dd} , U_{pd} result from linear combination of the interaction parameters (2.25), and the free parameter δ_{CT} accounts for charge-transfer. This double counting correction will act as a chemical potential for the d states in the Hamiltonian (2.40).

In solids, the Coulomb interaction is screened by the surrounding environment [30, Section 12]. The constrained random phase approximation (cRPA) [31] is a method to take this effect into account. Because this is an orbital-dependent procedure, predictions from the literature can only provide an order of magnitude estimate, so that empirical screening rules are used in practice, and especially F^0 is often treated as a free parameter [29, Section 2.5.2].

2.2.2 Green's functions in operator theory

Since the dimensionality of the problem can be significantly reduced by using mean-field methods and adding correlation effects explicitly only for a selected number of states, the many-body spectral problem $H|\psi\rangle = E|\psi\rangle$ is tractable and observables can be predicted as outlined in the beginning of Section 2. To develop the necessary theory for this, convenient mathematical language (e.g. [32]) is introduced in this section.

Let H be a bounded operator on a Hilbert-space \mathcal{H} . Then $z \in \mathbb{C}$ is said to be in the *resolvent set*, $z \in \rho(H) \stackrel{\text{def}}{\iff} (z - H)$ is a bijection with inverse $R_H(z) := (z - H)^{-1}$, which is called the *resolvent* of H in z . $\sigma(H) := \mathbb{C} \setminus \rho(H)$ is called the *spectrum* of H .

The Hilbert space \mathcal{H} is finite-dimensional in the numerical computations within this work, so that linear algebra (e.g. [33]), is sufficient to describe the spectral properties of operators on \mathcal{H} . Indeed, $\dim \mathcal{H} < \infty \iff \exists! n \in \mathbb{N}_0 : \mathcal{H} \cong \mathbb{C}^n$, and the spectrum of an operator H on this space is found as the set of values z for which the equation $H|\psi\rangle = z|\psi\rangle \iff (z - H)|\psi\rangle = 0$ has a non-trivial solution $\mathcal{H} \ni |\psi\rangle \neq 0 \iff \ker\{z - H\} \neq \{0\}$. This occurs if and only if (iff) $(z - H)$ is not injective, which is true iff⁴ $(z - H)$ is not bijective, *i.e.* $\det\{z - H\} = 0$. The last expression has as solutions the zeroes of a polynomial in z of degree n . According to the fundamental theorem of algebra, these are exactly n (not necessarily mutually distinct) isolated

⁴Note that this equivalence is generally valid *only in finite dimension*, which leads to an interesting spectral theory of operators on infinite-dimensional Hilbert-spaces, featuring, e.g., continuous spectrum [32].

points, called the *eigenvalues* of H . From the point of view of complex analysis, the eigenvalues of H are thus the poles of the resolvent $R_H(z) = (z - H)^{-1}$, which is a first motivation for the ubiquitous application of resolvent techniques in this thesis. Note that if $H = H^\dagger$, then $\sigma(H) \subset \mathbb{R}$, i.e. all poles of $R_H(z)$ lie on the real axis.

After choosing a particular basis $\mathcal{H} \supset (|i\rangle)_{i \in \Gamma}$ with $1_{\mathcal{H}} = \sum_{j \in \Gamma} |j\rangle \langle j| =: \int_{\Gamma} dj |j\rangle \langle j|$, and an operator H on \mathcal{H} , the map $\Gamma \times \Gamma \ni (i, j) \mapsto H_{ij} = \langle i | H | j \rangle \in \mathbb{C}$ is called the *kernel* of H in Γ -space. The name *kernel* is motivated by the “integral” kernel relation

$$\mathbb{C} \ni (H\psi)(i) := \langle i | H | \psi \rangle = \int_{\Gamma} dj \langle i | H | j \rangle \langle j | \psi \rangle = \int_{\Gamma} dj H_{ij} \psi(j), \quad \forall |\psi\rangle \in \mathcal{H}. \quad (2.27)$$

The *Green’s function* is defined as the kernel of the resolvent operator,

$$G_H(i, j; z) := \langle i | R_H(z) | j \rangle = \langle i | (z - H)^{-1} | j \rangle, \quad z \in \rho(H). \quad (2.28)$$

The significance of the resolvent is evident from its close connection to the time evolution via the Laplace transform \mathcal{L} of a state $|\psi(t)\rangle \in \mathcal{H}$.

$$\begin{aligned} \mathcal{L}(\mathcal{H}) \ni |\hat{\psi}(z)\rangle &= \int_0^\infty dt e^{izt} |\psi(t)\rangle \\ &= \int_0^\infty dt \underbrace{e^{izt} e^{-iHt}}_{e^{i(z-H)t}} |\psi(0)\rangle \\ &= \left. \frac{e^{i(z-H)t}}{i(z-H)} \right|_0^\infty |\psi(0)\rangle = \dots \end{aligned} \quad (2.29)$$

Note that convergence is guaranteed for $z = \omega + i\eta$, $\eta > 0$. The result can be expressed as a formal fraction of operators because numerator and denominator commute.

$$\begin{aligned} \dots &= -[i(z-H)]^{-1} |\psi(0)\rangle \\ &= i(z-H)^{-1} |\psi(0)\rangle. \end{aligned} \quad (2.30)$$

This argument will be used and generalized to predict arbitrary measurements of equilibrium observables in Section 2.3.1.

Using the distributional identity [34, Problem 1.3s]

$$\lim_{\eta \rightarrow 0^+} \frac{1}{x \pm i\eta} = \text{PV} \frac{1}{x} \mp i\pi\delta, \quad (2.31)$$

the language of Green’s functions also yields a convenient formulation for the (p)DOS (2.15):

$$\begin{aligned} pD_\phi(\omega) &= \sum_{nk} |\langle \phi | nk \rangle|^2 \delta(\omega - \epsilon_{nk}) \\ &= -\frac{1}{\pi} \lim_{\eta \rightarrow 0^+} \text{Im} \sum_{nk, mk'} \langle \phi | nk \rangle (\omega + i\eta - \epsilon_{nk})^{-1} \delta_{nk, mk'} \langle mk' | \phi \rangle \end{aligned}$$

$$\begin{aligned}
 &= -\frac{1}{\pi} \lim_{\eta \rightarrow 0^+} \text{Im} \sum_{nk, mk'} \langle \phi | \underbrace{|nk\rangle} \langle nk | (\omega + i\eta - h^{MF})^{-1} \underbrace{|mk'\rangle} \langle mk' | | \phi \rangle \\
 &= -\frac{1}{\pi} \lim_{\eta \rightarrow 0^+} \text{Im} G_{h^{MF}}(\phi, \phi, \omega + i\eta).
 \end{aligned} \tag{2.32}$$

The choice $|\phi\rangle = |mk'\rangle$ and summation over mk' according to (2.16) leads to the basis-independent formula

$$\begin{aligned}
 D(\omega) &= -\frac{1}{\pi} \lim_{\eta \rightarrow 0^+} \sum_{nk} \text{Im} G_{h^{MF}}(nk, nk, \omega + i\eta) \\
 &= -\frac{1}{\pi} \lim_{\eta \rightarrow 0^+} \text{Tr} \text{Im} R_{h^{MF}}(\omega + i\eta)
 \end{aligned} \tag{2.33}$$

for the DOS (2.14). In practical calculations η will be kept finite. Also this result will be generalized to an experimentally measurable spectral function (XAS) of a correlated system in Section 2.3.2.

2.2.3 Single Impurity Anderson Model

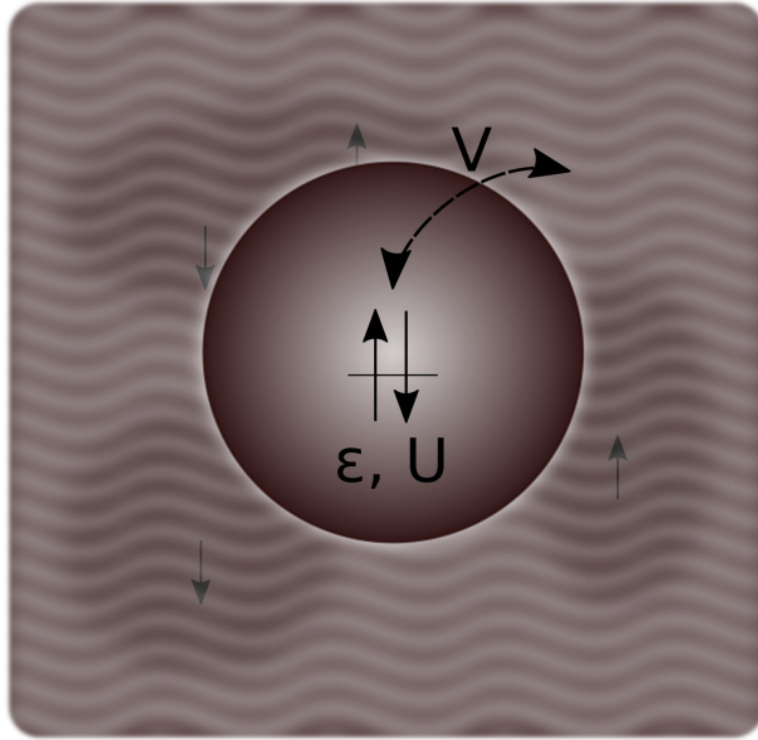


Figure 2.1: Schematic illustration of the SIAM. An impurity with explicit on-site correlations (circle) is coupled to a bath (background) that is treated on the mean-field level [35, Figure 1.8].

With the language of second quantization (Section 2.2.1) and Green's functions (Section 2.2.2) at hand, the Hamiltonian of the effective many-body model can be constructed explicitly. As

explained before, the aim is to treat as much of the system as possible on a mean-field level and only include explicit correlations where it is necessary, *i.e.* in a selected subspace of the full Hilbert space. The resolvent techniques developed in Section 2.2.2 provide an intuitive way to achieve this. The model resulting from this discussion is a single-impurity Anderson model (SIAM) [6], as illustrated in Figure 2.1.

Starting point is the resolvent of the mean-field Hamiltonian (2.10) expressed as a matrix in k -space:

$$g_k(z) = [z - h_k^{MF}]^{-1}, \quad z = (\omega + \mu + i\eta), \quad \eta = 0^+ \quad (2.34)$$

An effective model for a selected lattice site R is obtained by projection of this Green's function onto a relevant subspace of localized orbitals $|i\rangle$ at R from (2.18) with projection operators $P_{k,R} = \sum_i |k\rangle \langle k|i\rangle \langle i|$,

$$G_R(z) = \sum_k P_{k,R}^\dagger g_k(z) P_{k,R}. \quad (2.35)$$

The same is done for the mean-field Hamiltonian,

$$H_R = \sum_k P_{k,R}^\dagger h_k^{MF} P_{k,R}. \quad (2.36)$$

Note that the projected Green's function contains more information than the projected Hamiltonian as it also takes into account the effect of the bath on the impurity in terms of a hybridization function $\Delta_R(z)$:

$$G_R^{-1}(z) = [z - H_R - \Delta_R(z)], \quad \Delta_R(z) = z - H_R - G_R^{-1}(z). \quad (2.37)$$

$\Delta_R(z)$ describes how the propagation within the impurity-orbitals is modified due to hopping from an impurity orbital to the bath and back to an impurity-orbital.

This can be seen more clearly by writing the Hamiltonian in an explicit matrix form:

$$H = \left(\begin{array}{c|ccc} H_R & & & V \\ \hline & \epsilon_1 & & \\ V^\dagger & & \epsilon_2 & \\ & & & \ddots \end{array} \right) \quad (2.38)$$

with H_R a Hermitian $n \times n$ matrix for n impurity orbitals, ϵ a real and diagonal $m \times m$ matrix for m bath states, and V an $n \times m$ matrix of hopping amplitudes between the two subspaces.

The Green's function in the subspace of the impurity is then given by

$$G_R(z) = (z - H)^{-1} \Big|_R$$

$$\begin{aligned}
 &= \left(\begin{array}{c|c} z - H_R & -V \\ \hline -V^\dagger & z - \epsilon \end{array} \right)^{-1} \Big|_R \\
 &= (z - H_R - \underbrace{V(z - \epsilon)^{-1}V^\dagger}_{\equiv \Delta_R(z)})^{-1}.
 \end{aligned} \tag{2.39}$$

A small number of bath states per impurity orbitals is often enough to capture the essential features of the hybridization function $\Delta_R(z)$ as obtained from (2.37) [6]. After fitting the corresponding bath energies ϵ and hoppings V , explicit interaction terms U can be added in the manner of Section 2.2.1. For the concrete application to 2p→3d excitations at Ti in this work, the resulting effective Hamiltonian can be expressed as [6, Section B]:

$$\begin{aligned}
 H = & \sum_{ij} \epsilon_{d_{i,j}} d_i^\dagger d_j + \sum_i \epsilon_{b_i} b_i^\dagger b_i + \sum_{ij} V_{i,j} (d_j^\dagger b_i + b_i^\dagger d_j) \\
 & + \sum_{ijkl} U_{ijkl}^{dd} d_i^\dagger d_j^\dagger d_l d_k - \sum_i \Sigma_{DC} d_i^\dagger d_i + \sum_{ijkl} U_{ijkl}^{pd} d_i^\dagger p_j^\dagger p_l d_k \\
 & + \sum_i \epsilon_p p_i^\dagger p_i + \xi_p \sum_{ij} \langle p_i | l \cdot s | p_j \rangle p_i^\dagger p_j,
 \end{aligned} \tag{2.40}$$

where p^\dagger, d^\dagger create states in p,d-orbitals on the impurity, b^\dagger creates a state in the bath. Note that a finite spin-orbit coupling strength ξ for the p-orbitals is added as an explicit relativistic correction and Σ_{DC} according to (2.26) is used to compensate double-counting of the mean-field part of the interaction.

2.3 Calculation of observables: Linear Response Theory

The prediction of macroscopic observables from microscopic principles is a central aim of materials theory (Section 1.1). This connection is established in the framework of Linear Response Theory (e.g. [28, Section 5,6,8]) using Green's function methods [34].

2.3.1 Green's functions as correlation functions

Let a physical system be described by the Schrödinger Hamiltonian $H_{S,0}$ and density matrix $\rho_{S,0} = Z_0^{-1} e^{-\beta H_{S,0}}$, $Z_0 = \text{Tr} e^{-\beta H_{S,0}}$ in equilibrium at time $t \rightarrow -\infty$. Consider a perturbation $V_S = f(t) \cdot B_S$, where B_S is a Schrödinger operator and $f(t)$ a classical function of time with $f(t \rightarrow -\infty) = 0$. Suppose, the experimental setup is designed so that changes in the observable A are measured: $\Delta A(t) = \text{Tr}\{\rho_S(t)A_S\} - \text{Tr}\{\rho_{S,0}A_S\}$, with $\rho_S = Z^{-1} e^{-\beta H_S}$, $Z = \text{Tr} e^{-\beta H_S}$. Then, to linear order in f , the experimental outcome will be:

$$\Delta A(t) = \int dt' G_{A,B}^r(t, t') f(t'), \tag{2.41}$$

where the retarded Green's function associated to A and B is defined as

$$\begin{aligned} G_{A,B}^r(t, t') &= -i\theta(t - t') \underbrace{\text{Tr}\left\{\rho_{S,0}[A_{H,0}(t), B_{H,0}(t')]\right\}}_{=:\langle [A_{H,0}(t), B_{H,0}(t')]_{-\zeta} \rangle} \\ &= \theta(t - t') \left\{ \underbrace{-i\langle A_{H,0}(t)B_{H,0}(t') \rangle}_{=:G_{AB}^>(t, t')} - (-\zeta) \underbrace{i\langle B_{H,0}(t')A_{H,0}(t) \rangle}_{=:G_{AB}^<(t, t')} \right\}, \end{aligned} \quad (2.42)$$

with $\zeta = \pm 1$ for bosonic (fermionic) operators and the subscript $H, 0$ indicating the Heisenberg picture w.r.t. $H_{S,0}$. This result is known as the Kubo formula (detailed discussion and proof e.g. in [28, Section 6.1]). Note that to first order in the coupling field f , the non-equilibrium expectation value can indeed be evaluated in terms of equilibrium observables, which is a remarkable result. The retarded Green's function enforces causality and is a first-order expression in correlators $\langle AB \rangle$. By cyclicity of the trace and the fact that $\rho_{S,0}$ commutes with the time-evolution operator $U = e^{-itH_{S,0}}$, $G_{A,B}^r(t, t') = G_{A,B}^r(t - t')$, which is a manifestation of time-translation invariance of the system in equilibrium. Note that because A is an observable/Hermitian, f is a real function, and the integral measure in (2.41) is real, also $G_{A,B}^r(t - t')$ has to be real-valued.

In order to relate this to the resolvent operator introduced in Section 2.2.2, Laplace transform $G_{AB}^+(t) = \theta(t)G_{AB}^>(t)$ [36, Section 1] with $z = \omega + i\eta$:

$$\begin{aligned} G_{AB}^+(z) &= -i \int dt e^{izt} G_{AB}^+(t) \\ &= -i \int_0^{+\infty} dt e^{izt} \langle A(t)B(0) \rangle = \dots, \end{aligned} \quad (2.43)$$

and by taking the trace in the many-body eigenbasis $|n\rangle$ of H ,

$$\begin{aligned} \dots &= -i \int_0^{+\infty} dt e^{izt} \sum_n \frac{e^{-\beta E_n}}{Z} \langle n | e^{iHt} A e^{-iHt} B | n \rangle \\ &= -i \int_0^{+\infty} dt \sum_n \frac{e^{-\beta E_n}}{Z} \langle n | A e^{i(z+E_n-H)t} B | n \rangle = \dots \end{aligned} \quad (2.44)$$

Because the decay is sufficient for $\eta > 0$, one may commute summation with integration and arrive at

$$\dots = -i \sum_n \frac{e^{-\beta E_n}}{Z} \langle n | A \frac{e^{i(z+E_n-H)t}}{i(z+E_n-H)} \Big|_0^{+\infty} B | n \rangle = \dots \quad (2.45)$$

Note that this result may be written formally as a fraction of operators, because numerator and denominator commute in this case.

$$\dots = \sum_n \frac{e^{-\beta E_n}}{Z} \langle n | A \underbrace{[z + E_n - H]^{-1}}_{=:R_H(z+E_n)} B | n \rangle \quad (2.46)$$

finally shows the connection to the resolvent operator from Section 2.2.2. Similarly, one finds for $G_{AB}^-(t) = \theta(t)G_{AB}^<(t)$,

$$G_{AB}^-(z) = \sum_n \frac{e^{-\beta E_n}}{Z} \langle n | A \underbrace{[-z + E_n - H]^{-1}}_{=R_H(-z+E_n)} B | n \rangle. \quad (2.47)$$

For the retarded Green's function, this means:

$$\begin{aligned} G_{A,B}^r(z) &= G_{AB}^+(z) - (-\zeta)G_{AB}^-(z) \\ &= \sum_n \frac{e^{-\beta E_n}}{Z} \langle n | A \underbrace{[z + E_n - H]^{-1} - (-\zeta)[-z + E_n - H]^{-1}}_{=R_H^r(z)} B | n \rangle. \end{aligned} \quad (2.48)$$

It is instructive to introduce identities $\mathbb{1} = \sum_m |m\rangle \langle m|$ to further evaluate R_H^r in the many-body eigenbasis of H :

$$\begin{aligned} G_{A,B}^r(z) &= \sum_{n,m,l} \frac{e^{-\beta E_n}}{Z} \langle n | A | m \rangle \underbrace{\langle m | R_H^r(z) | l \rangle}_{=\langle m | R_H^r(z) | m \rangle \delta_{m,l}} \langle l | B | n \rangle \\ &= \sum_{n,m} \frac{e^{-\beta E_n}}{Z} \langle n | A | m \rangle \langle m | B | n \rangle \langle m | R_H^r(z) | m \rangle \\ &= \sum_{n,m} \frac{e^{-\beta E_n}}{Z} |\langle n | A | m \rangle|^2 \langle m | R_H^r(z) | m \rangle, \quad (A^\dagger = A = B) \end{aligned} \quad (2.49)$$

for the highly relevant case of common operators.

The matrix elements of the retarded resolvent in the many-body eigenbasis of H are

$$\langle m | R_H^r(z) | m \rangle = \frac{1}{\omega + i\eta + E_n - E_m} - (-\zeta) \frac{1}{-\omega - i\eta + E_n - E_m}, \quad (2.50)$$

so that the imaginary part of (2.49) is identified as

$$\begin{aligned} \text{Im}\{G_{A,A}^r(z)\} &= -\pi \sum_{n,m} \frac{e^{-\beta E_n}}{Z} |\langle n | A | m \rangle|^2 \\ &\quad \times [L_\eta(\omega + E_n - E_m) - (-\zeta)L_\eta(-\omega + E_n - E_m)], \end{aligned} \quad (2.51)$$

where $L_\eta(E) = \frac{1}{\pi\eta} \frac{\eta^2}{E^2 + \eta^2}$ is a Lorentzian peak at $E = 0$ with scale parameter η (half width at half maximum). Note that the contribution from G_{AA}^+ is peaked at energies $\omega + E_n = E_m$ (*absorptive*) while the contribution from G_{AA}^- is peaked at $-\omega + E_n = E_m$ (*emissive*).

By interchanging n and m in the second term, it can be seen that for large frequencies $\omega\beta \gg 1$, the thermal occupation factor separates the sum over many-body states into two practically distinct sets of initial and final states respectively:

$$\text{Im}\{G_{A,A}^r(z)\} = -\pi \sum_{n \in I, m \in F} \frac{e^{-\beta E_n} - (-\zeta)e^{-\beta E_m}}{Z} |\langle n | A | m \rangle|^2 L_\eta(\omega + E_n - E_m)$$

$$\approx -\pi \sum_{n \in I, m \in F} \frac{e^{-\beta E_n}}{Z} |\langle n | A | m \rangle|^2 L_\eta(\omega + E_n - E_m), \quad (2.52)$$

so that only the absorptive part arising from G_{AA}^+ survives. In the computationally convenient [37] notation of (2.46),

$$\text{Im}\{G_{A,A}^r(z)\} \approx \sum_{n \in I} \frac{e^{-\beta E_n}}{Z} \text{Im} \langle n | A [\omega + i\eta + E_n - H]^{-1} A | n \rangle. \quad (2.53)$$

In practice, the operators in this equation will be furthermore restricted to the relevant subspaces $I(F)$ of initial(final) states respectively, thereby replacing A by a non-hermitian operator *a posteriori*,

$$\text{Im}\{G_{A,A}^r(z)\} \approx \sum_n \frac{e^{-\beta E_n}}{Z} \text{Im} \langle n | A^\dagger [\omega + i\eta + E_n - H]^{-1} A | n \rangle. \quad (2.54)$$

2.3.2 Transition rate in an external field

As an explicit example [11, Section 7], consider the coupling of a system to an external electromagnetic field,

$$H' = H + f_\omega(t)T, \quad (2.55)$$

with $f_\omega(t) = \text{Re}\{E_0 e^{iz^*t}\}$ for a monochromatic field, which is adiabatically turned on in the distant past, $z^* = \omega - i\eta$. In dipole approximation in the regime of x-ray absorption [38, Section 4.1], $T \propto \epsilon \cdot p$, where ϵ is the light polarization vector and p the momentum operator.

The aim is to calculate the rate of energy transfer between the system and the external field,

$$\dot{Q}_\omega = \left\langle \frac{\partial H'}{\partial t} \right\rangle = \dot{f}_\omega(t) \langle T_H(t) \rangle. \quad (2.56)$$

An average over a full cycle of the field oscillation $\Delta t = \frac{2\pi}{\omega}$ yields

$$\begin{aligned} \overline{\dot{Q}_\omega} &= \frac{1}{\Delta t} \int_0^{\Delta t} dt \dot{f}_\omega(t) \langle T_H(t) \rangle \\ &= \frac{1}{\Delta t} \int_0^{\Delta t} dt \dot{f}_\omega(t) \left[\langle T_H(-\infty) \rangle + \int dt' G_{TT}^r(t-t') f_\omega(t') \right] = \dots \end{aligned} \quad (2.57)$$

Neglecting terms of order η , the equilibrium part $\langle T_H(-\infty) \rangle$ is averaged out,

$$\begin{aligned} \dots &= \frac{1}{\Delta t} \int_0^{\Delta t} dt \dot{f}_\omega(t) \int dt' G_{TT}^r(t-t') f_\omega(t') + o(\eta) \\ &\approx \frac{1}{4\Delta t} \int_0^{\Delta t} dt \left(i\omega E_0 e^{iz^*t} - i\omega E_0^* e^{-izt} \right) \int dt' G_{TT}^r(t-t') \underbrace{\left(E_0 e^{iz^*t'} + E_0^* e^{-izt'} \right)}_{=\tau} + o(\eta) \\ &\approx \frac{1}{4\Delta t} \int_0^{\Delta t} dt \left(i\omega E_0 e^{iz^*t} - i\omega E_0^* e^{-izt} \right) \int d\tau G_{TT}^r(\tau) \left(E_0 e^{iz^*(t-\tau)} + E_0^* e^{-iz(t-\tau)} \right) = \dots, \end{aligned} \quad (2.58)$$

Recognize the Laplace transform of the Green's function,

$$G_{TT}^r(z) = \int d\tau G_{TT}^r(\tau) e^{iz\tau}, \quad G_{TT}^r(-z^*) = \int d\tau G_{TT}^r(\tau) e^{-iz^*\tau} = G_{TT}^r(z)^*, \quad (2.59)$$

because $G_{TT}^r(\tau)$ is real according to the Kubo formula. Therefore,

$$\dots = \frac{1}{4\Delta t} \int_0^{\Delta t} dt \left(i\omega E_0 e^{iz^*t} - i\omega E_0^* e^{-izt} \right) \left(E_0 G_{TT}^r(z)^* e^{iz^*t} + E_0^* G_{TT}^r(z) e^{-izt} \right) = \dots \quad (2.60)$$

Due to $\frac{1}{\Delta t} \int_0^{\Delta t} dt e^{inz t} = \delta_{n,0} + o(\eta)$, $n \in \mathbb{Z}$, only terms $\sim |E_0|^2$ survive,

$$\begin{aligned} \dots &= i\omega \frac{|E_0|^2}{4} [G_{TT}^r(z)^* - G_{TT}^r(z)] + o(\eta) \\ &\approx \omega \frac{|E_0|^2}{2} \frac{1}{2i} [G_{TT}^r(z) - G_{TT}^r(z)^*] \\ &= \omega \frac{|E_0|^2}{2} \text{Im}\{G_{TT}^r(z)\}. \end{aligned} \quad (2.61)$$

Since \bar{Q}_ω describes the rate of energy transfer at frequency ω , $\bar{Q}_\omega \propto \text{Im}\{G_{TT}^r(z)\}$ is proportional to the rate μ_ω of corresponding many-body excitations (each costing the energy ω^5), thereby recovering a generalized version of Fermi's golden rule through (2.51).

Combining this result with (2.54) from Section 2.3.1 ($\beta\omega \gg 1$ is valid in the regime of XAS), the transition rate measured in XAS experiments can be efficiently predicted as

$$\mu_\omega \sim \sum_n \frac{e^{-\beta E_n}}{Z} \text{Im} \langle n | T^\dagger [\omega + E_n - (H - i\Gamma)]^{-1} T | n \rangle. \quad (2.62)$$

Note that the *infinitesimal* decay parameter $\eta = 0^+$ in (2.54) – introduced to simulate adiabatic coupling to an external source (2.55) and hence make the Laplace transform of the Green's function (2.43) convergent – has been absorbed in a *finite* decay parameter Γ in the space of final states $m \in F$, which has been introduced *a posteriori*⁶. This free parameter accounts for decay of the final states according to $e^{-i(H-i\Gamma)t} |m\rangle = e^{-iE_m t} e^{-\Gamma t} |m\rangle$ via channels that the present model does not capture. The effect on the resulting spectra is a Lorentzian peak-broadening according to (2.52).

⁵Since this work does not employ a quantum-field-theoretic description of the environment, this part of the argument has to remain semi-classical: Even though coupling to an external source was introduced in terms of a classical field $f(t)$, the quantum nature of light is used as an additional input.

⁶How the decay channels can be introduced consistently *a priori* remains unaddressed in this work, but would be an interesting extension of the project. It is clear that the derivations reviewed here rely on Hermiticity of the Hamiltonian, so that one cannot naïvely add an imaginary decay matrix to the Hamiltonian in the beginning.

2.4 Phonons and electron-phonon coupling

To take into account the effect of lattice vibrations on the electronic structure [28, Section 3], expand the inter-ionic potential around its equilibrium position, $R = R_0 + u_R$. Because the equilibrium position is an energetic minimum by definition, the linear term vanishes and one obtains

$$\begin{aligned} V_{\text{ion}} &= \sum_{R_0 \neq R'_0} V(R - R') \\ &= \sum_{R_0 \neq R'_0} V(R_0 - R'_0) + \frac{1}{2} \sum_{R_0 \neq R'_0, \mu\nu} u_R^\mu \left. \frac{\partial^2 V}{\partial u_R^\mu \partial u_{R'}^\nu} \right|_{u=0} u_{R'}^\nu + o(u^3) \\ &= \sum_{R_0 \neq R'_0} V(R_0 - R'_0) + \frac{1}{2} \sum_{q, \mu\nu} u_{-q}^\mu V_{q\mu\nu}^{(2)} u_q^\nu + o(u^3), \end{aligned} \quad (2.63)$$

after transformation to Fourier space. The *dynamical matrix* $V_{q\mu\nu}^{(2)}$ is symmetric and can therefore be diagonalized in an orthonormal basis of modes $u_{q\lambda}$ with eigenvalues $M\omega_{q\lambda}^2$, where λ is a polarization index. Note that in insulators such as STO, a dipole-interaction contribution to the dynamical matrix gives rise to a splitting between the longitudinal and transversal optical branches (LO-TO splitting) [39].

After bosonic quantization, the resulting phonon Hamiltonian reads

$$H_{ph} = \sum_{q\lambda} \omega_{q\lambda} \left(b_{q\lambda}^\dagger b_{q\lambda} + \frac{1}{2} \right), \quad (2.64)$$

and the displacement operator in real space is given by

$$u_R(t) = \sum_{q\lambda} \left(\frac{1}{2MN\omega_{q\lambda}} \right)^{\frac{1}{2}} (b_{q\lambda} u_{q\lambda} e^{-i\omega_{q\lambda}t} + b_{-q\lambda}^\dagger u_{-q\lambda} e^{i\omega_{q\lambda}t}) e^{iqR_0}. \quad (2.65)$$

For later reference, note that for $q \rightarrow 0$ (Γ -point of the Brillouin zone), and after restriction to a single mode $u_{0\lambda}$, the displacement scales as

$$u_{R0\lambda} \propto M^{-\frac{1}{2}} u_{0\lambda}, \quad (2.66)$$

where M is the mass of the ion at position R .

Harmonic expansion of V_{ext} around the equilibrium positions in terms of the introduced phonon modes makes the interaction between electrons and phonons of the form $\sim c_{k+q}^\dagger c_k (b_q + b_{-q}^\dagger)$ apparent, which is also the starting point for the BCS theory of superconductivity [28, Section 3.6].

Within this work, the electron-phonon interaction will be treated in adiabatic approximation, *i.e.* the atomic displacements due to a phonon mode $q\lambda$ will be used as *parameters* in (2.4), and the electronic observables will be calculated for different values of the displacement (frozen phonon model).

3 Computational Methods

This section contains details about the implementation of the theoretical methods explained in Section 2. Following the workflow diagram Figure 1.4, the starting point of the numerical study is an experimental structure of STO in the cubic phase, obtained as a .cif-file from the ICSD database [13]. Using the code cif2cell [40], this document is converted into a format suitable for the electronic structure code RSPt.

3.1 RSPt

RSPt [41] is an implementation of DFT using a LMTO basis as described in Section 2.1. The code can be obtained from [42] after registration via e-mail to rspt.admin@physics.uu.se. RSPt is here used to calculate the density of states (2.32,2.33), the local Hamiltonian (2.36) and hybridization function (2.37) for the Ti 3d orbitals in STO, as well as the spin-orbit coupling ξ for the p-orbitals and most of the interaction parameters in the Hamiltonian (2.40). An introduction to the code is given in the selection of tutorials [43]. Calculations within this work are based on these and use their default settings if not else specified. A linear grid of $12 \times 12 \times 12$ k-points is used to sample the Brillouin zone. For all quantities extracted from the mean-field Green's-function, the energy axis is sampled by 1001 linear points from -1 Ryd to 1 Ryd. The distance from the real axis is chosen as $\eta = 0.01$ Ryd, and the SIAM is constructed within an energy window of -0.4 Ryd to 0.7 Ryd. The calculations were executed on the high performance computer cluster Rackham [44], using up to 20 cores for one hour.

3.2 rspt2spectra

rspt2spectra [45] implements the discretization of the hybridization function as described in Section 2.2.3 and acts as an interface between RSPt and impurityModel (Section 3.3). 3-4 bath states per impurity orbital were fitted in energy-windows selected by hand to capture the essential features of the hybridization function. Output of the calculation is the non-interacting, non-relativistic part of the Hamiltonian (2.40). Because this part of the calculation is not very expensive, execution on a personal computer is sufficient.

3.3 impurityModel

The code impurityModel [46] implements the calculation of the XA spectral function (2.62). It takes as input the Hamiltonian constructed by rspt2spectra and adds the significant spin-orbit coupling and interaction-terms to arrive at (2.40). With the notation d for an electron in a

d-orbital and \underline{b} for a hole in the bath, the configurations $d^{n_{\underline{b}}}\underline{b}^{n_{\underline{b}}}$, $n_{\underline{b}} = 0, 1, 2$ are taken into account to construct the lowest energy-eigenstates $|n\rangle$ using the Lanczos-algorithm [29, Appendix A]. The XA spectral function is calculated for a range of incoming photon energies and for different polarization directions. The absolute position of the spectrum – corresponding to the energy of the core orbitals – is not respected in this implementation, but later fitted to experimental data. The temperature was set to $T = 300$ K and a peak broadening $\Gamma = 0.05$ eV was used to account for the decay of the final states, but also to resolve differences in the spectra due to lattice distortions. The spin-orbit coupling and interaction parameters are listed in Table 3.1.

F_{dd}^0	F_{dd}^2	F_{dd}^4	F_{pd}^0	F_{pd}^2	G_{pd}^1	G_{pd}^3	δ_{CT}	ξ_p
5.19	8.57	6.02	6.0	4.20	2.73	1.54	1.5	3.83

Table 3.1: Computational parameters used in the impurityModel calculation, all values in eV.

The heavily screened F_{dd}^0 is approximated by a literature result [47], F_{pd}^0 and δ_{CT} are extrapolated from the trend in [6, Table 1]. F_{dd}^2 and F_{dd}^4 are empirically [6] screened by 0.82, 0.88 of their RSPT values. All other values are directly obtained from RSPT.

The calculations were performed on the high performance computer cluster Tetralith [48] on up to 64 cores for up to 3 hours.

4 Results and Discussion

In order to validate the construction of the theory on the mean-field level, this Section will start out by comparing the electronic structure obtained from DFT calculations in this work to previous experimental and theoretical results on STO in the bulk [49]. These investigations have shown that STO is an insulator with a direct band gap of 3.75 eV and indirect band gap of 3.25 eV, which is consistent with the observation from Section 1.2 that pure STO is perceived as transparent in the visible regime with an energy range of roughly 1.5 – 3.25 eV [50]. It is well known [49, Section III.C.] that DFT in the LDA (2.7) tends to underestimate the band gap of STO by about 1.5 eV, so that one would expect to see a gap of ~ 1.75 eV = 0.13 Ryd in the DOS at the LDA level, which is discussed in detail below.

4.1 Density of states

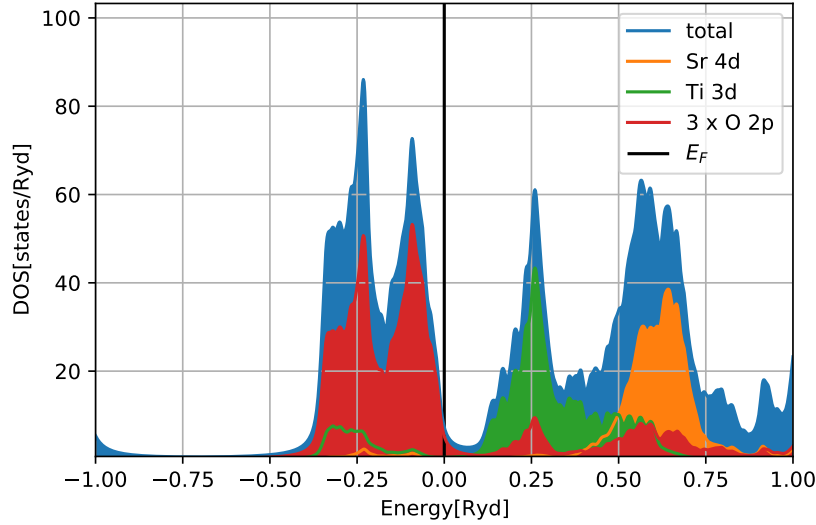


Figure 4.1: DOS and pDOS of STO calculated with RSPt via (2.32). The contribution of the Sr 4d, Ti 3d and O 2p orbitals are shown as pDOS for the corresponding sites.

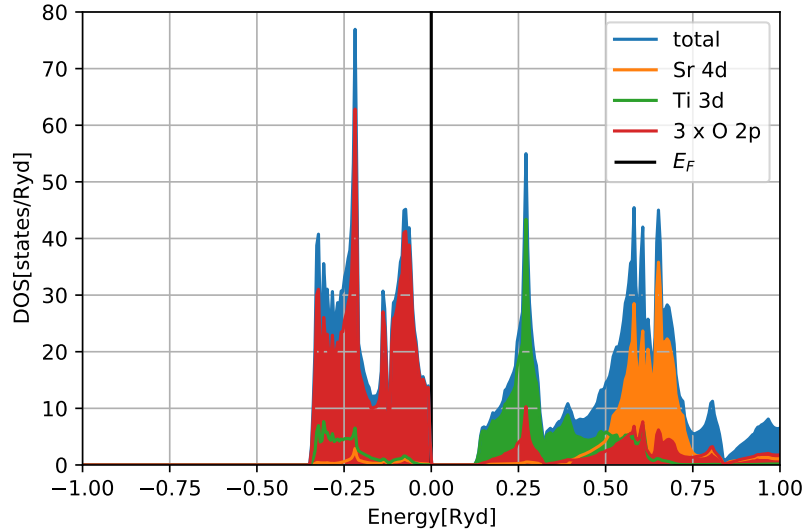


Figure 4.2: DOS and pDOS of STO calculated with RSPt using an implementation of (2.15).

Figure 4.1 shows the (p)DOS (2.32),(2.33) of STO as obtained from RSPt. The results reproduce the qualitative features in previous literature [49, Figure 11] well. Around $E_F = 0$, Figure 4.1 shows a non-vanishing density of states, which is an effect of Lorentzian tails resulting from the imaginary offset $\eta = 0.01$ Ryd. Effectively decreasing $\eta \rightarrow 0$ by direct integration of (2.15), also

the density of states goes to zero at the Fermi energy (Figure 4.2), and an indirect band gap of ~ 0.13 Ryd is observed as anticipated before.

Convergence of the electronic structure with respect to the number of k-points was verified by increasing to $24 \times 24 \times 24$ and comparing the resulting pDOS to the data shown here. The essential features did not change visibly, so that reasonable convergence can be assumed. Since the hybridization function (2.37) will also be calculated from the Green's function (2.34), Figure 4.1 allows for an estimate of the main hybridization contributions for the local Ti 3d orbitals. This is how the energy window (-0.4 Ryd to 0.7 Ryd) for construction of the SIAM is motivated.

4.2 Phonon spectrum and lattice modulation

This section discusses the adiabatic phonon modulation in STO (experimental setup similar to Figure 1.2) assuming a pump peaked around a frequency of 3 THz (Figure 4.3).

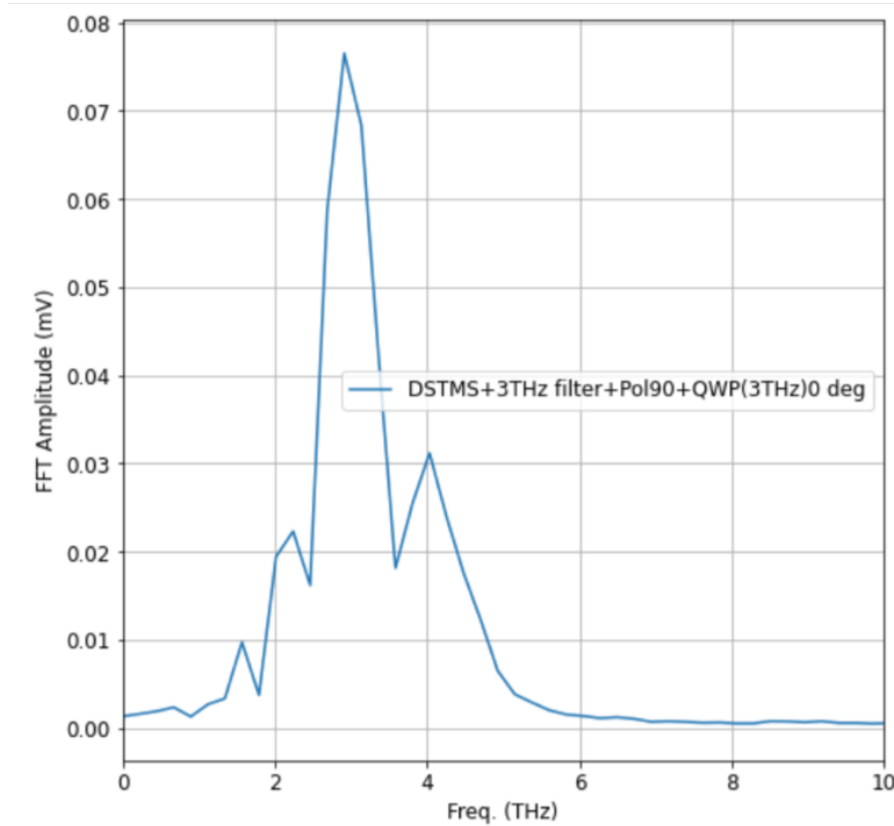


Figure 4.3: Frequency spectrum of an experimental pump pulse peaked around 3 THz [by courtesy of Stefano Bonetti].

To identify which phonon modes are excited by this pump, the dominant resonant modes are identified in the phonon spectrum of STO shown in Figure 4.4.

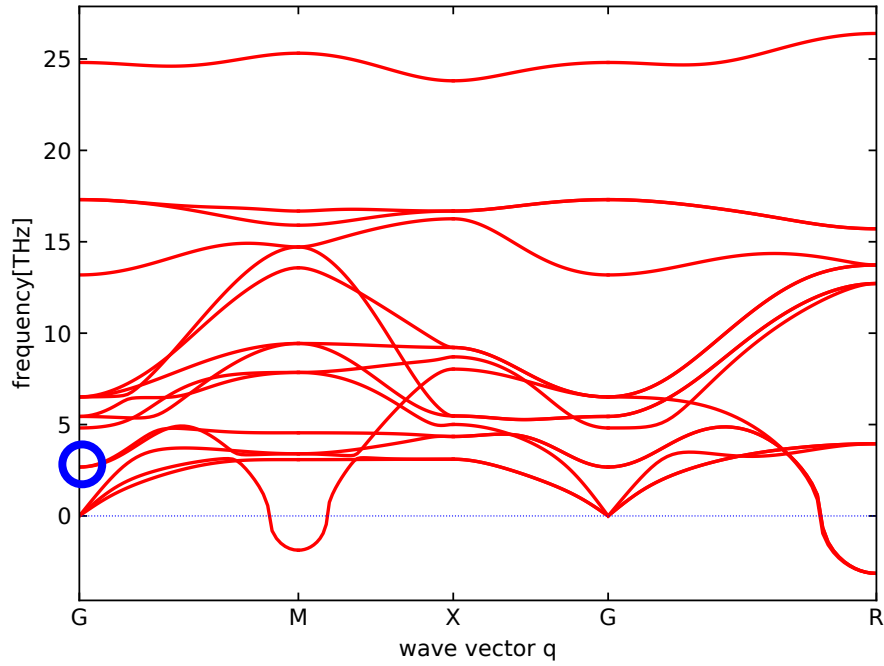


Figure 4.4: Phonon band structure of STO obtained from VASP[51]+phonopy[52] calculations [by courtesy of Xin Shen]. A term correction [39] was applied to account for long-range dipole-dipole interactions, so that the longitudinal and transversal optical phonon branches split. Negative frequencies around M and R indicate unstable imaginary modes driving the structural phase-transition to a tetragonal structure below 105K (Section 1.2). Neglecting the momentum transferred by a photon in comparison to the size of the Brillouin zone, a pump peaked around 3 THz would excite the pair of degenerate transversal optical modes at $(q \rightarrow 0, 2.68 \text{ THz})$ (blue circle).

The frequencies in the phonon spectrum presented here do not completely agree with previously reported data in the literature. [1, Figure 1a and Supplementary Information] based on earlier experimental data [53, 54, 55] finds a lowest optical frequency of 0.93 THz at Γ , but points out that the frequency of this mode depends sensitively on temperature [56]. [57, Figure 2] predicts an instability at the Γ -point. Since the phonon modulation is here treated on an adiabatic level, only the symmetry of the distorted structure (not so much the phonon frequency) is relevant in the steps following, and a more detailed analysis of the discrepancies in the phonon spectra will be postponed.

Taking into account the mass-normalization (2.66) of the corresponding eigenvectors, an atomic displacement in real space for one of the degenerate phonon modes at ($q \rightarrow 0$, 2.68 THz) is calculated from the phonopy output and illustrated in Figure 4.5.

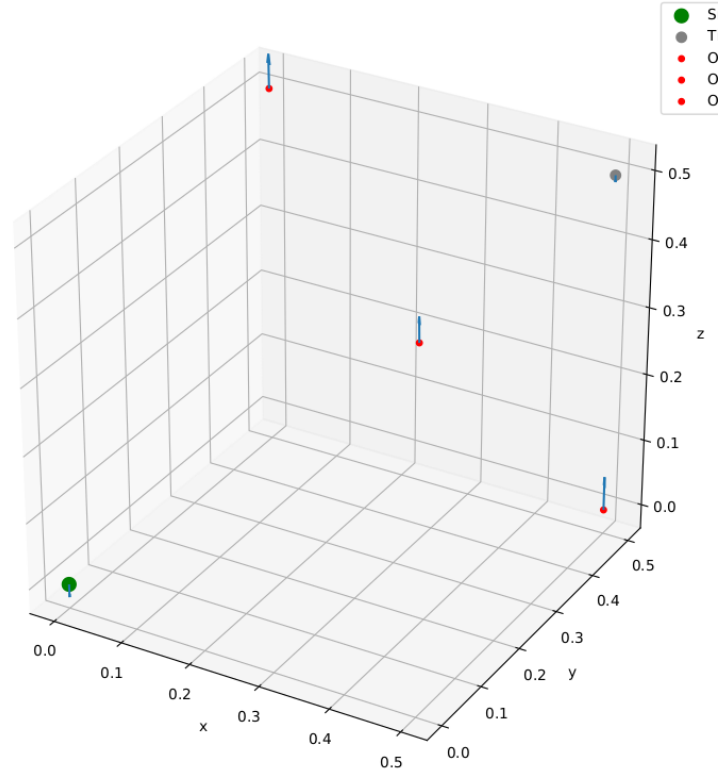


Figure 4.5: Atomic displacements (blue arrows) corresponding to a transversal optical phonon mode at ($q \rightarrow 0$, 2.68 THz). Coordinates are normalized to the lattice parameter 3.9 Å of the cubic unit cell [13]. The maximum displacement is set to $\delta = 5\%$, which is a guess based on experimental investigations [1]. Different sizes of the spheres indicate their mass ratio.

4.3 Discretization of the hybridization function

Figure 4.6 shows the hybridization functions (2.37) of the Ti 3d orbitals in a basis of cubic harmonics (e_g and t_{2g} orbitals) as calculated with RSPT for the experimental crystal structure [13] of STO, and for the structure distorted according to Figure 4.5. The e_g orbitals (d_{z^2} and $d_{x^2-y^2}$) hybridize more strongly with the environment than the t_{2g} orbitals ($d_{yz, xz, xy}$), which is consistent with the crystal structure shown in Figure 1.1.

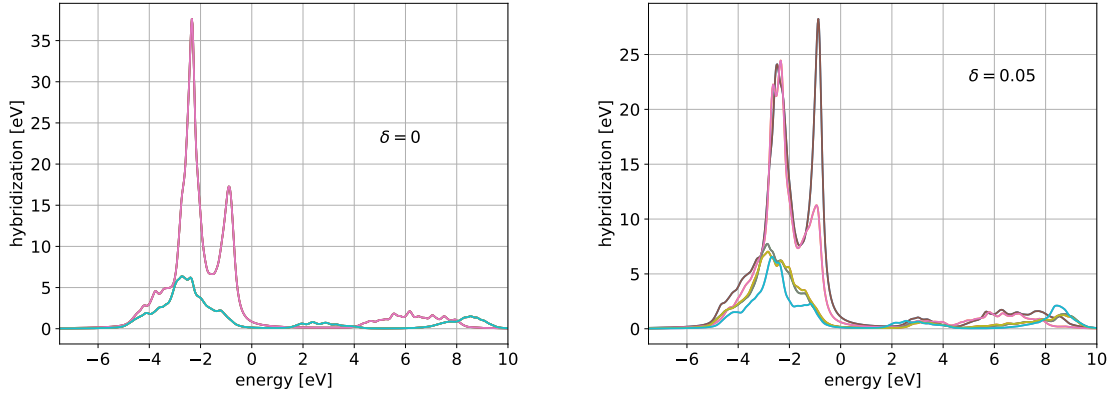


Figure 4.6: Diagonal part of the hybridization functions calculated with RSPt. The offdiagonal elements vanish in the undistorted case and are ~ 1 eV in the distorted case. Left: Hybridization of e_g orbitals (violet) and t_{2g} orbitals (blue) in the cubic structure, *i.e.* displacement $\delta = 0$. Right: $\delta = 5\%$ maximum displacement. The two e_g orbitals (d_{z^2} brown, $d_{x^2-y^2}$ violet) are clearly inequivalent.

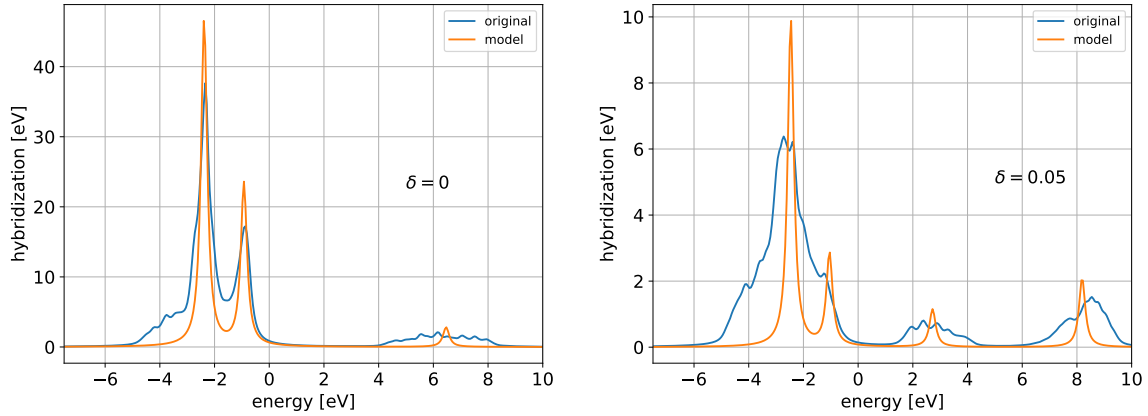


Figure 4.7: Discretization of the hybridization function in the undistorted case by fitting both energies and hopping parameters to its imaginary part. Left: e_g orbitals. Right: t_{2g} orbitals.

The discretization of the diagonal elements of the hybridization function with `rspt2spectra` according to Section 2.2.3 is shown in Figure 4.7 for the undistorted case, and in Figure 4.8 for a $\delta = 5\%$ distortion. The energy windows were selected to achieve a good fit in the undistorted case and then also used for the distorted case to make the results comparable. Optimizing the fit separately for the distorted case only leads to minor changes in the resulting spectra and

does not change the final interpretations.

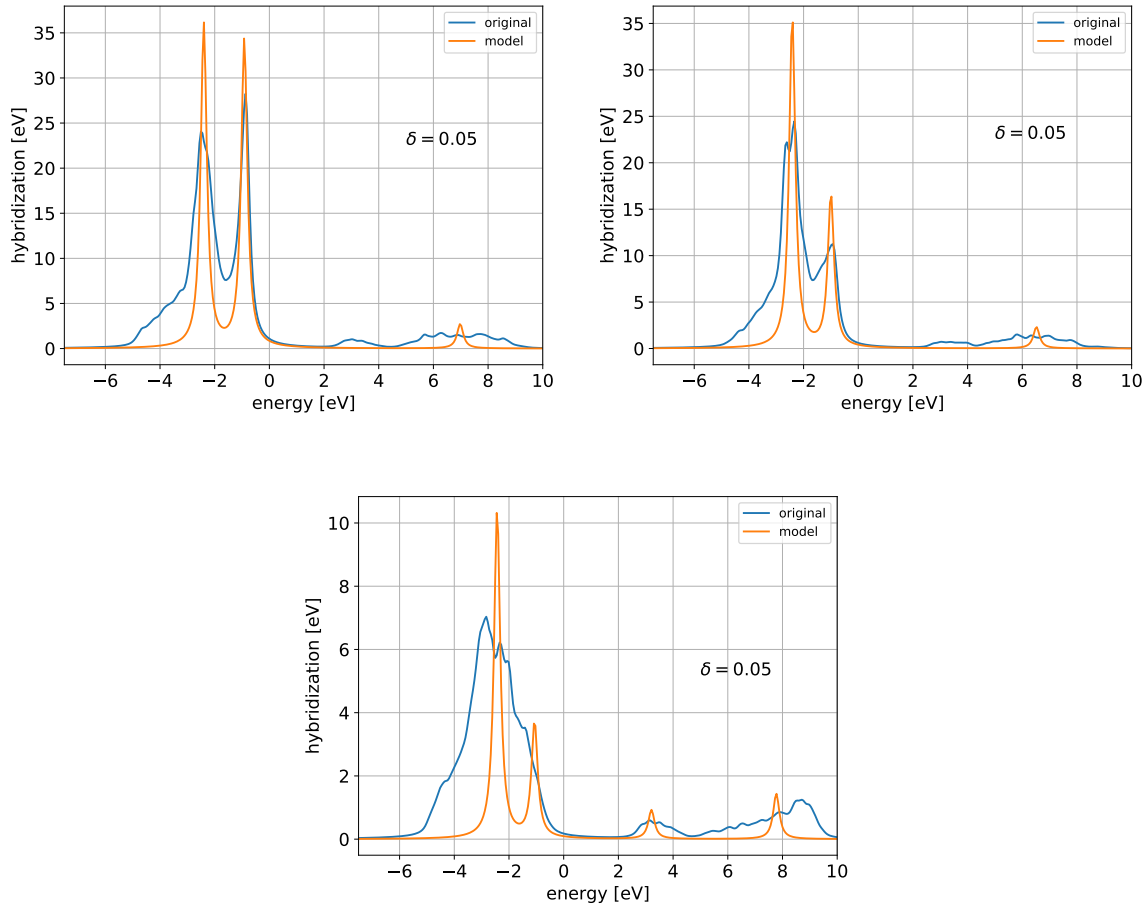


Figure 4.8: Discretization of the hybridization function in the case of $\delta = 5\%$ distortion. Upper row: e_g orbitals d_{z^2} (left) and $d_{x^2-y^2}$ (right) with visible differences in hybridization. Lower plot: one of the (practically equivalent) t_{2g} orbitals.

Whereas the hybridization matrix is diagonal in the undistorted case, the phonon distortion breaks the local octahedral symmetry, which leads to small off-diagonal elements (~ 1 eV). Most importantly, the two e_g orbitals are not any more degenerate, and their hybridization with the O 2p orbitals below the Fermi level (see DOS Figure 4.1) changes significantly.

4.4 X-ray absorption spectra

After construction of the SIAM (2.40) with the output from `rspt2spectra` and the parameters specified in Table 3.1, the calculation of the x-ray absorption spectral function (2.62) with `impurityModel` yields the results shown in Figure 4.9 for octahedral symmetry ($\delta = 0$).

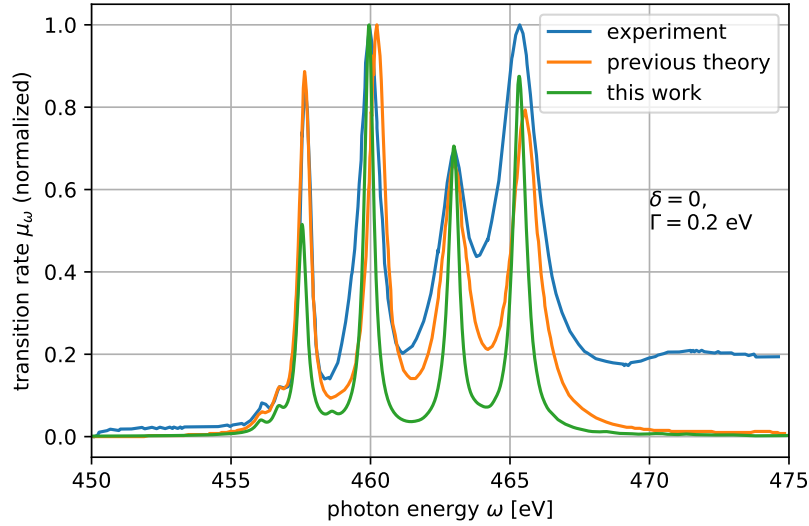


Figure 4.9: XAS of STO for $\delta = 0$ with peak broadening $\Gamma = 0.2$ eV in comparison to data digitized from previous experimental [58, Figure 1] and previous theoretical [5, Figure 7] work.

Especially the peak position reproduces well previous experimental and previous theoretical results. The shape of the spectrum is typical for the $L_{2,3}$ -edge of nominally d^0 compounds in octahedral symmetry [4, Section C]. The constant lifetime-broadening $\Gamma = 0.2$ eV underestimates the values observed in experiment for almost all peaks. In the following analysis, however, it will be decreased even further to resolve any sensitivity of the spectra to phonon modulations.

Whereas the relative intensity of most of the peaks is satisfactory and confirms the choice of parameters, the intensity of the first peak is clearly underestimated. However, the results shown here are not very sensitive to the free parameters in Table 3.1, as also previously reported for other materials [6]. This is an indication that the approach used in this work underestimates the absolute value of the crystal field parameter $10Dq$, which is a standard parameter in atomic multiplet calculations describing the splitting of e_g and t_{2g} orbitals in the non-interacting limit [38]. As [4, Figure 3] suggests, a larger absolute value $10Dq$ would increase the intensity of the first peak. Due to the presence of strong correlations in the system, this would happen in a non-linear way. In this approach, $10Dq$ is not a free parameter, but the effect of the crystal field is taken into account by the hybridization function (2.37). In principle, one could compensate the underestimated crystal-field splitting by adding a correction term with cubic symmetry to $\epsilon_{d_{i,j}}$ in (2.40), but at the cost of introducing an additional free parameter to the theory. Another option would be to try if another projection scheme for obtaining a local basis set (ORT [26]) is more suitable to capture the crystal field effect correctly or if the choice of free parameters can

be slightly improved. Since the main interest of this work is however in *relative* changes of the XAS after distortions, the absolute precision of the results is not crucial.

According to the group-theoretical arguments in [4, Sections C,D], breaking the octahedral symmetry by a phonon modulation should lead to further splitting parameters as well as polarization-dependence in the XA spectra.

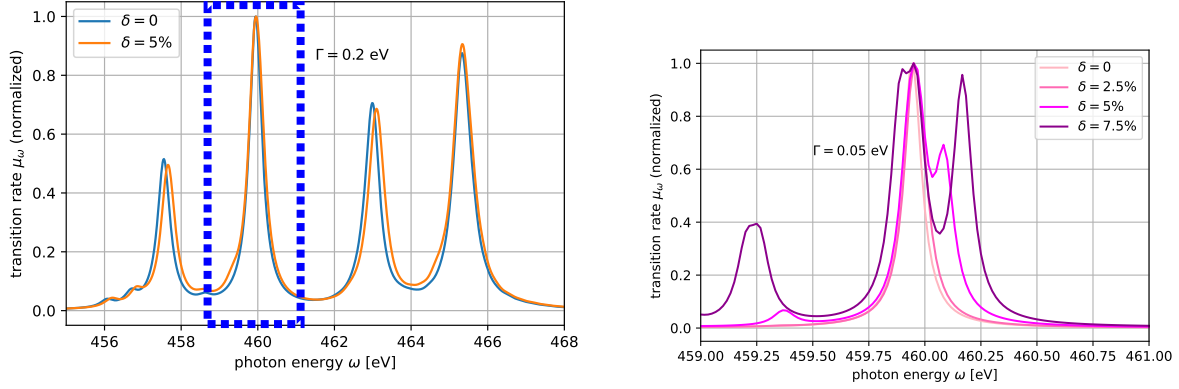


Figure 4.10: Phonon modulated XAS of STO. Left: Full view for $\Gamma = 0.2$ eV. In the distorted case, additional shoulders emerge on the previously observed peaks. Right: Detailed view of the second large peak (blue rectangle in the left panel) for reduced broadening $\Gamma = 0.05$ eV. δ increases with intensity of the color.

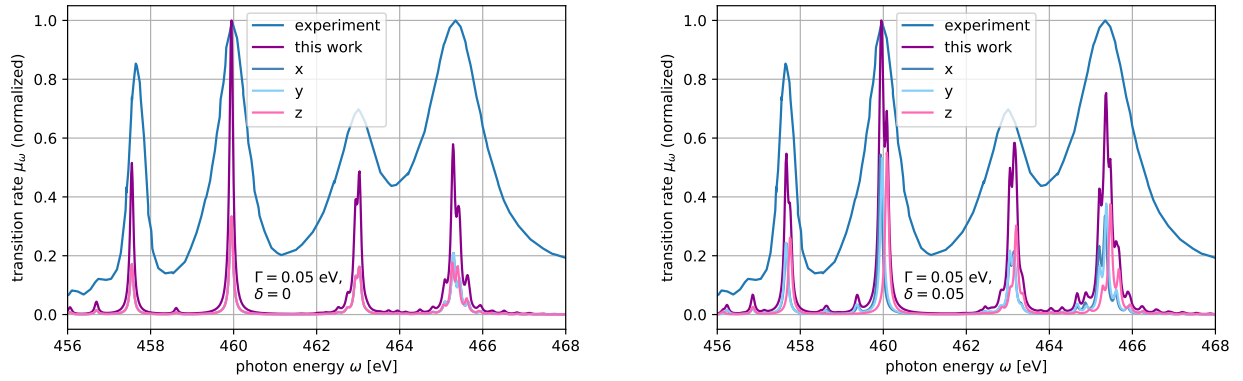


Figure 4.11: Polarization dependence in XAS of STO. In the case of octahedral symmetry ($\delta = 0$, left panel), all polarization directions are equivalent within numerical precision. Breaking the octahedral symmetry ($\delta = 5\%$, right panel), a nontrivial polarization dependence is observed in the simulated spectra. Experimental data [58, Figure 1] measured on the undistorted structure is shown for reference in both panels.

Figure 4.10 shows the effect of the phonon modulation (Figure 4.5) on the XAS results as predicted by RSPt+impurityModel. One can deduce that with increasing δ , the peaks split and new features emerge in a nonlinear way. This is in agreement with the discussion in [4, Section C]: just as the crystal-field splitting 10Dq causes a branching from spherical to octahedral symmetry, lowering the symmetry further down (e.g. to c_{4v}) leads to additional branching effects. Also the polarization dependence anticipated in [4, Section D] is observed, as reported in Figure 4.11.

4.5 Experimental applications

A natural experimental application of this work would be the attempt to detect the signatures predicted in Figures 4.10, 4.11 by forcing large coherent displacements in the lattice using a pump-probe setup as sketched in Figure 1.2.

Even though Figure 4.11 indicates that the experimental resolution from 1996 [58, Figure 1] would not be sufficient to resolve the changes in the spectra (the experimental peak broadening is large compared to the peak splittings), some changes of the features clearly exceed thermal effects ($\sim kT = 0.025$ eV), and are just in reach of state of the art experimental resolution (~ 0.1 eV [59]). In addition, one could exploit the polarization-dependence of the spectra and compare measurements with different probe-polarizations in order to isolate the changes more reliably. The short life-time of the core-hole, $\frac{\hbar}{\tau} = \Gamma \sim 0.1$ eV [16, Section 2.1.2]), remains the fundamentally limiting factor. Including the most relevant decay channels in the calculations would permit a more precise, energy-dependent estimate of the peak-broadening.

The theoretical simulations in this work predict potentially observable changes in the XAS of STO even for small coherent distortions in the lattice structure, which reflects the strong susceptibility of the electronic structure to excitations of the crystal lattice. Experimental XAS measurements on phonon-modulated STO could not only be used to test this direct result, but also to test the applicability of the adiabatic approximation to phonon-modulations in STO in general, and therefore validate further theoretical studies of other modulated observables, such as the dielectric tensor in the optical regime.

5 Conclusion

In this work, the Multiplet Ligand Field Theory approach [5, 6] was used to analyse the influence of phonon modulations [1] on the x-ray absorption near-edge fine structure of the Ti-L_{2,3}-edge in SrTiO₃. Previous experimental [58] and previous theoretical [5] data on the

cubic structure were reproduced with good agreement. Even small phonon modulations with a maximum atomic displacement of 5% of the unit cell were shown to cause potentially observable, polarization-dependent changes in the x-ray absorption spectra. This illustrates the strong effect of lattice modulations on the electronic structure of SrTiO_3 .

The intensity of the first large peak in the absorption spectrum was underestimated in comparison to experiments, which is indication that the crystal-field splitting $10Dq$ is underestimated in the construction of the single-impurity Anderson model. One should check if another RSPT projection scheme (ORT [26]) is more suitable to capture the crystal field effect correctly, or if modifications in the fit of the hybridization function and free parameters are needed. At the cost of introducing an additional free parameter to the theory, one could even add a correction term with cubic symmetry to $\epsilon_{d_{i,j}}$ in (2.40).

A detailed understanding of the x-ray absorption spectra in the symmetry-broken structure in terms of selection rules and group theory is still outstanding, but desired to check and support the numerical simulations. To reduce the complexity of this analysis, one could restrict it to $T = 0$ and then discuss the transition matrix elements under branching of octahedral symmetry to, e.g., c_{4v} .

Including the relevant decay-channels of the core-hole in the calculations would be a way to give a more reliable estimate of the energy-dependent peak-broadening.

An experimental test of the predictions made here, namely *polarization-dependent changes in the x-ray absorption spectral function of SrTiO_3 as a result of collective lattice excitations*, is desirable also to validate further theoretical predictions of other observables in the frozen phonon approximation.

As this work will be continued collaboratively in Uppsala and Heidelberg until September 2021, there might also be time to start an investigation on resonant inelastic x-ray spectroscopy by collective *magnetic* excitations, based on [26, 60]. In combination with the work presented here, this analysis could be a contribution to the understanding of how x-ray-spectroscopy can be used to investigate collective spin- and lattice- excitations in real materials. From an educational point of view, the theoretical workflow (Figure 1.4) applied here seems to be easily transferable to other problems in modern materials theory and is therefore an excellent introduction into this field of research.

Acknowledgments

This work was organizationally and financially supported through scholarships by **Erasmus+** and **Cusanuswerk e.V.**

I am deeply grateful to my supervisors **Maurits Haverkort** and **Olle Eriksson** for their joint effort to make this work possible as a collaborative project. This is not only a benefit for my academic education, but also a valuable experience for life.

Many thanks to **Oscar Grånäs** and **Patrik Thunström** for their proposals, patience, support, and feedback on a daily basis. Each of you is a great supervisor, and I enjoyed it even more to work with the two of you in combination.

I want to thank my colleagues **Kristofer Björnson**, **Johan Jönsson**, **Chin Shen Ong**, and **Xin Shen** for their contributions to this work through input, theoretical discussions, and computational troubleshooting. Furthermore, I thank **Stefano Bonetti** and **Sergei Butorin** for their input from the experimental point of view, **Susanne Mirbt** for her readiness to examine this work on short notice, and the Erasmus physics team, **Dimitri Arvanitis** and **Rabab Elkarib**, for help with the formal aspects.

A big thank you to the whole **materials theory division** for providing this inspiring and caring environment for successful research and education!

For helping me to cope with the challenges of living abroad, I want to thank Freja W. and the people at Uppsala ju-jutsuklubb (ujjk), who made me feel at home in Uppsala, as well as Benwermarna for offering great dancing courses when it was still possible, and for stopping them at a sensible time in the interest of protecting ourselves as well as other people.

Last but not least, I thank my family and friends in Germany for their continuous love and support before and during my stay in Sweden (hopefully also beyond). I am grateful and happy to have you as a good reason to come back home.

List of Figures

1.1	STO crystal structure	4
1.2	Pump-probe experiment	5
1.3	XA process $2p \rightarrow 3d$	6
1.4	Research strategy	7
2.1	Schematic illustration of the SIAM	16
4.1	DOS and pDOS of STO, via Green's function	26
4.2	DOS and pDOS of STO, directly integrated	26
4.3	Frequency spectrum of a THz pump pulse	27
4.4	Phonon band structure of STO	28
4.5	Atomic displacements	29
4.6	Hybridization functions	30
4.7	Discretization of the hybridization function, undistorted case	30
4.8	Discretization of the hybridization function, distorted case	31
4.9	XAS of STO	32
4.10	Phonon modulated XAS of STO	33
4.11	Polarization dependence in XAS of STO.	33

List of Tables

3.1	impurityModel parameters	25
-----	------------------------------------	----

References

- [1] Michael Kozina et al. “Terahertz-driven phonon upconversion in SrTiO₃”. In: *Nature Physics* 15.4 (2019), pp. 387–392.
- [2] T Yamaguchi, S Shibuya, S Suga, and S Shin. “Inner-core excitation spectra of transition-metal compounds: II. pd absorption spectra”. In: *Journal of Physics C: Solid State Physics* 15.12 (1982), p. 2641.
- [3] BT Thole, RD Cowan, GA Sawatzky, J Fink, and JC Fuggle. “New probe for the ground-state electronic structure of narrow-band and impurity systems”. In: *Physical Review B* 31.10 (1985), p. 6856.
- [4] FMF De Groot, JC Fuggle, BT Thole, and GA Sawatzky. “L_{2,3} x-ray-absorption edges of d⁰ compounds: K⁺, Ca²⁺, Sc³⁺, and Ti⁴⁺ in O_h (octahedral) symmetry”. In: *Physical Review B* 41.2 (1990), p. 928.
- [5] MW Haverkort, M Zwierzycki, and OK Andersen. “Multiplet ligand-field theory using Wannier orbitals”. In: *Physical Review B* 85.16 (2012), p. 165113.
- [6] Johann Lüder et al. “Theory of L-edge spectroscopy of strongly correlated systems”. In: *Physical Review B* 96.24 (2017), p. 245131.
- [7] Nick Smith. “The Seven Ages of Materials”. In: *Engineering & Technology* 14.9 (2019), pp. 22–25.
- [8] WH Butler, X-G Zhang, TC Schulthess, and JM MacLaren. “Spin-dependent tunneling conductance of Fe| MgO| Fe sandwiches”. In: *Physical Review B* 63.5 (2001), p. 054416.
- [9] Sining Mao et al. “Commercial TMR heads for hard disk drives: characterization and extendibility at 300 gbit²”. In: *IEEE transactions on magnetics* 42.2 (2006), pp. 97–102.
- [10] Uppsala University. *Materials for Sustainable Energy Solutions*. URL: <https://www.physics.uu.se/research/materials-theory/ongoing-research/materials-for-sustainable-energy-solutions/> (visited on 2020-01-25).
- [11] Paul M Chaikin, Tom C Lubensky, and Thomas A Witten. *Principles of condensed matter physics*. Vol. 10. Cambridge university press Cambridge, 1995.
- [12] Mindat.org mineralogy database. *Tausonite*. 2002. URL: <https://www.mindat.org/min-3895.html> (visited on 2020-12-21).
- [13] GM Meyer, RJ Nelmes, and J Hutton. “High-resolution (direct space) studies of anharmonic motion associated with the structural phase transition in SrTiO₃”. In: *Ferroelectrics* 21 (1978), pp. 461–462.

- [14] Koichi Momma and Fujio Izumi. “VESTA 3 for three-dimensional visualization of crystal, volumetric and morphology data”. In: *Journal of applied crystallography* 44.6 (2011), pp. 1272–1276.
- [15] Q Song et al. “Evidence of cooperative effect on the enhanced superconducting transition temperature at the FeSe/SrTiO₃ interface”. In: *Nature communications* 10.1 (2019), pp. 1–8.
- [16] Frank d. Groot and Akio Kotani. *Core level spectroscopy of solids*. Vol. 6. Boca Raton: CRC Press, 2008.
- [17] Lev Davidovich Landau, Evgenij Mihajlovič Lifšic, Evgenii Mikhailovich Lifshitz, and LP Pitaevskii. *Statistical physics: theory of the condensed state*. Vol. 9. Butterworth-Heinemann, 1980.
- [18] John M Wills et al. *Full-Potential Electronic Structure Method: energy and force calculations with density functional and dynamical mean field theory*. Vol. 167. Springer Science & Business Media, 2010.
- [19] Lev D. Landau and Evgenij M. Lifšic. *Quantum mechanics: non-relativistic theory*. Vol. 3. London: Pergamon Press, 1958.
- [20] Richard M Martin. *Electronic structure: basic theory and practical methods*. Cambridge university press, 2020.
- [21] Patrik Thunström. “Correlated Electronic Structure of Materials: Development and Application of Dynamical Mean Field Theory”. PhD thesis. Acta Universitatis Upsaliensis, 2012.
- [22] Kerson Huang. *Statistical mechanics*. 2. New York: Wiley, 1987.
- [23] Pierre Hohenberg and Walter Kohn. “Inhomogeneous electron gas”. In: *Physical review* 136.3B (1964), B864.
- [24] Walter Kohn and Lu Jeu Sham. “Self-consistent equations including exchange and correlation effects”. In: *Physical review* 140.4A (1965), A1133.
- [25] Neil W. Ashcroft and N. D. Mermin. *Solid state physics*. Saunders College, 1976.
- [26] Yaroslav O Kvashnin et al. “Exchange parameters of strongly correlated materials: Extraction from spin-polarized density functional theory plus dynamical mean-field theory”. In: *Physical Review B* 91.12 (2015), p. 125133.
- [27] Richard Feynman. *Statistical mechanics: a set of lectures*. advanced book classics, 1998.

- [28] Henrik Bruus and Karsten Flensberg. *Many-body quantum theory in condensed matter physics: an introduction*. Oxford university press, 2004.
- [29] Johan Schött. “Theoretical and Computational Studies of Strongly Correlated Electron Systems: Dynamical Mean Field Theory, X-ray Absorption Spectroscopy and Analytical Continuation”. PhD thesis. Acta Universitatis Upsaliensis, 2018.
- [30] Alexander L. Fetter and John Dirk Walecka. *Quantum theory of many-particle systems*. eng. Corr. repr. Mineola, N.Y.: Dover Publ., 2003, XVI, 601 S.
- [31] F Aryasetiawan, Krister Karlsson, O Jepsen, and U Schönberger. “Calculations of Hubbard U from first-principles”. In: *Physical Review B* 74.12 (2006), p. 125106.
- [32] Michael Reed and Barry Simon. *Methods of modern mathematical physics. vol. 1. Functional analysis*. Academic San Diego, 1980.
- [33] Siegfried Bosch. *Lineare Algebra*. ger. 5., überarb. u. erweiterte Aufl. 2014. SpringerLink: Bücher. Berlin, Heidelberg: Springer Spektrum, 2014, Online-Ressource (X, 385 S, online resource). URL: <http://dx.doi.org/10.1007/978-3-642-55260-1>.
- [34] Eleftherios N Economou. *Green’s functions in quantum physics*. Vol. 7. Springer Science & Business Media, 2006.
- [35] Johan Jönsson. *Electronic transitions and correlation effects: From pure elements to complex materials*. Vol. 2053. Linköping University Electronic Press, 2020.
- [36] Peter Schmitteckert. “Calculating Green functions from finite systems”. In: *Journal of Physics: Conference Series*. Vol. 220. 1. IOP Publishing. 2010, p. 012022.
- [37] Y Lu, M Höppner, O Gunnarsson, and MW Haverkort. “Efficient real-frequency solver for dynamical mean-field theory”. In: *Physical Review B* 90.8 (2014), p. 085102.
- [38] FMF De Groot. “X-ray absorption and dichroism of transition metals and their compounds”. In: *Journal of Electron Spectroscopy and Related Phenomena* 67.4 (1994), pp. 529–622.
- [39] Xavier Gonze, J-C Charlier, DC Allan, and MP Teter. “Interatomic force constants from first principles: The case of α -quartz”. In: *Physical Review B* 50.17 (1994), p. 13035.
- [40] Torbjörn Björkman. “CIF2Cell: Generating geometries for electronic structure programs”. In: *Computer Physics Communications* 182.5 (2011), pp. 1183–1186.
- [41] J.M. Wills et al. *RSPT*. 2017. URL: <https://www.physics.uu.se/research/materials-theory/ongoing-research/code-development/rspt-main/> (visited on 2020-12-07).
- [42] J.M. Wills et al. *RSPT v1.1 2017*. 2017. URL: <https://github.com/uumaterialstheory/rspt> (visited on 2020-09-07).

- [43] Johan Schött. *RSpt-tutorials*. 2018. URL: <https://github.com/RSpt-tutorials> (visited on 2020-09-07).
- [44] Uppsala Multidisciplinary Center for Advanced Computational Science (UPPMAX). *Rackham*. URL: <https://uppmx.uu.se/support/user-guides/rackham-user-guide/> (visited on 2020-12-17).
- [45] Johan Schött. *rspt2spectra*. 2018. URL: <https://github.com/JohanSchott/rspt2spectra> (visited on 2020-09-25).
- [46] Johan Schött. *impurityModel*. 2018. URL: <https://github.com/JohanSchott/impurityModel> (visited on 2020-09-25).
- [47] Joseph W Bennett et al. “A systematic determination of hubbard U using the GBRV ultrasoft pseudopotential set”. In: *Computational Materials Science* 170 (2019), p. 109137.
- [48] National Supercomputer Centre at Linköping University. *Tetralith*. URL: <https://www.nsc.liu.se/systems/tetralith/> (visited on 2020-12-17).
- [49] K Van Benthem, C Elsässer, and RH French. “Bulk electronic structure of SrTiO₃: Experiment and theory”. In: *Journal of applied physics* 90.12 (2001), pp. 6156–6164.
- [50] DH Sliney. “What is light? The visible spectrum and beyond”. In: *Eye* 30.2 (2016), pp. 222–229.
- [51] Georg Kresse and Jürgen Furthmüller. “Efficient iterative schemes for ab initio total-energy calculations using a plane-wave basis set”. In: *Physical review B* 54.16 (1996), p. 11169.
- [52] A Togo and I Tanaka. “First principles phonon calculations in materials science”. In: *Scr. Mater.* 108 (2015), pp. 1–5.
- [53] RA Cowley. “Lattice dynamics and phase transitions of strontium titanate”. In: *Physical Review* 134.4A (1964), A981.
- [54] VN Denisov, BN Mavrin, VB Podobedov, and JF Scott. “Hyper-Raman spectra and frequency dependence of soft mode damping in SrTiO₃”. In: *Journal of Raman spectroscopy* 14.4 (1983), pp. 276–283.
- [55] AS Barker Jr. “Temperature Dependence of the Transverse and Longitudinal Optic Mode Frequencies and Charges in SrTiO₃ and BaTiO₃”. In: *Physical Review* 145.2 (1966), p. 391.
- [56] Premysl Marsik et al. “Terahertz ellipsometry study of the soft mode behavior in ultrathin SrTiO₃ films”. In: *Applied Physics Letters* 108.5 (2016), p. 052901.

- [57] Michael Porer et al. “Ultrafast Relaxation Dynamics of the Antiferrodistortive Phase in Ca Doped SrTiO₃”. In: *Physical review letters* 121.5 (2018), p. 055701.
- [58] Y Uehara. “Resonant inelastic scattering at the L edge of Ti in Barium Strontium Titanate by soft X-ray fluorescence spectroscopy”. In: *Applied Physics A* 65.2 (1996).
- [59] Daniel J Higley et al. “Femtosecond X-ray magnetic circular dichroism absorption spectroscopy at an X-ray free electron laser”. In: *Review of scientific instruments* 87.3 (2016), p. 033110.
- [60] MW Haverkort. “Theory of resonant inelastic X-ray scattering by collective magnetic excitations”. In: *Physical review letters* 105.16 (2010), p. 167404.